energies

Article

# Model Predictive Control-Enabled Primary Frequency Support for Variable-Speed Pumped Storage with Mechanical Constraints

**Kien Nguyen *, Evan Franklin, Michael Negnevitsky, Alan Henderson and Waqas Hassan**

School of Engineering, University of Tasmania, Sandy Bay, TAS 7005, Australia; evan.franklin@utas.edu.au (E.F.); michael.negnevitsky@utas.edu.au (M.N.); alan.henderson@utas.edu.au (A.H.); waqas.hassan@utas.edu.au (W.H.)
* Correspondence: vtkn@utas.edu.au

**Abstract**

Pumped hydro storage (PHS) systems, increasingly deployed in power systems with large shares of wind and solar generation, can play a key role in managing power system frequency. Variable-speed pumped hydro storage (VS-PHS) systems, in particular, have potential for rapid primary frequency response by enabling the quick release of machine rotor kinetic energy. However, using conventional proportional–integral (PI) control for converters and governors can result in large speed deviations and torque imbalance during fast system transients. This issue is intensified in PHS plants with slow hydraulic response, such as those with long penstocks or slow guide-vane adjustments, potentially violating mechanical operating constraints. This paper develops a model predictive control (MPC) strategy for coordinated governor and converter control, accounting for operational constraints. The proposed approach improves coordination of hydraulic and electrical systems, utilising DC-link storage and proactive guide-vane action for rapid power adjustments. Dynamic simulations using a complex nonlinear plant demonstrate that MPC redistributes energy extraction between the DC-link storage and the rotating mass while respecting their imposed limits. Furthermore, robustness tests indicate that MPC performance is sustained under plant nonlinearities and measurement noise. These results highlight the advantages of predictive control for supporting frequency response in VS-PHS systems.

**Keywords:** model predictive control; pumped storage; primary frequency control; variable-speed pumped hydro storage; converter-fed synchronous machines

## 1. Introduction

The increasing penetration of intermittent renewable energy sources is driving a greater need for fast and reliable frequency control in power systems. Large-scale energy storage facilities are essential to balance active power fluctuations and ensure secure system operation under rapid changes in supply and demand [1]. Among these, pumped hydro storage (PHS) remains the most widely deployed technology worldwide owing to its high capacity, long service life, and proven operational reliability [2]. Recent developments in power electronic converters have enabled variable-speed PHS (VS-PHS) units, which offer greater operational flexibility than conventional fixed-speed designs [3]. This flexibility allows for independent control of active and reactive power, improved efficiency over a wider operating range, and better integration with variable renewable generation [3–5]. As a result, variable-speed configurations are increasingly considered for future installations as part of the transition to low-carbon power systems.



Academic Editor: Bertrand Raison

Received: 12 June 2026
Revised: 3 July 2026
Accepted: 10 July 2026
Published: 14 July 2026

In addition to their efficiency and flexibility advantages, VS-PHS plants are a potential solution for primary frequency control (PFC). Power electronic converters in VS-PHS plants can be controlled to enable rapid power injection or absorption in response to grid frequency deviations, using the kinetic energy from machine rotors [6,7]. The structure of a VS-PHS unit with full back-to-back converters, illustrated in Figure 1, consists of the turbine–machine set, machine-side converter, DC link and grid-side converter. In normal operation, control responsibilities are distributed across three main stages. First, the grid-side converter ensures the desired amount of power is supplied to the grid from the DC link. Meanwhile, the machine-side converter manages power transfer from the machine to the DC link in order to maintain a constant DC-link voltage, which will in turn result in a slowing down or speeding up of the machine rotor. Finally, the turbine governor system ensures that speed is always returned to its setpoint by adjusting turbine mechanical input power via guide-vane position. During frequency events requiring fast power adjustments, a conventional control structure, based on separate control loops for rotational speed and DC-link voltage, keeps the DC-link voltage rigidly at its setpoint. However, in units with long penstocks, water acceleration is slow, causing hydraulic governors to lag behind the fast electrical response. The converters and DC-link capacitors can react on a millisecond timescale, whereas the guide vane and hydraulic flow head transient may require several seconds to effectively increase turbine mechanical power. This timescale mismatch in the dynamic response of the subsystems is illustrated in Figure 1. The mismatch causes the DC-link voltage regulator to extract power almost instantaneously from the rotating mass. Consequently, most of the transient demand is met by kinetic energy prior to the turbine power increases, leading to large rotational speed deviations, increased rotor acceleration and shaft torque imbalance (the difference between mechanical torque exerted by the turbine and electrical counter-torque provided by the machine) and potential hydraulic instabilities [8,9].

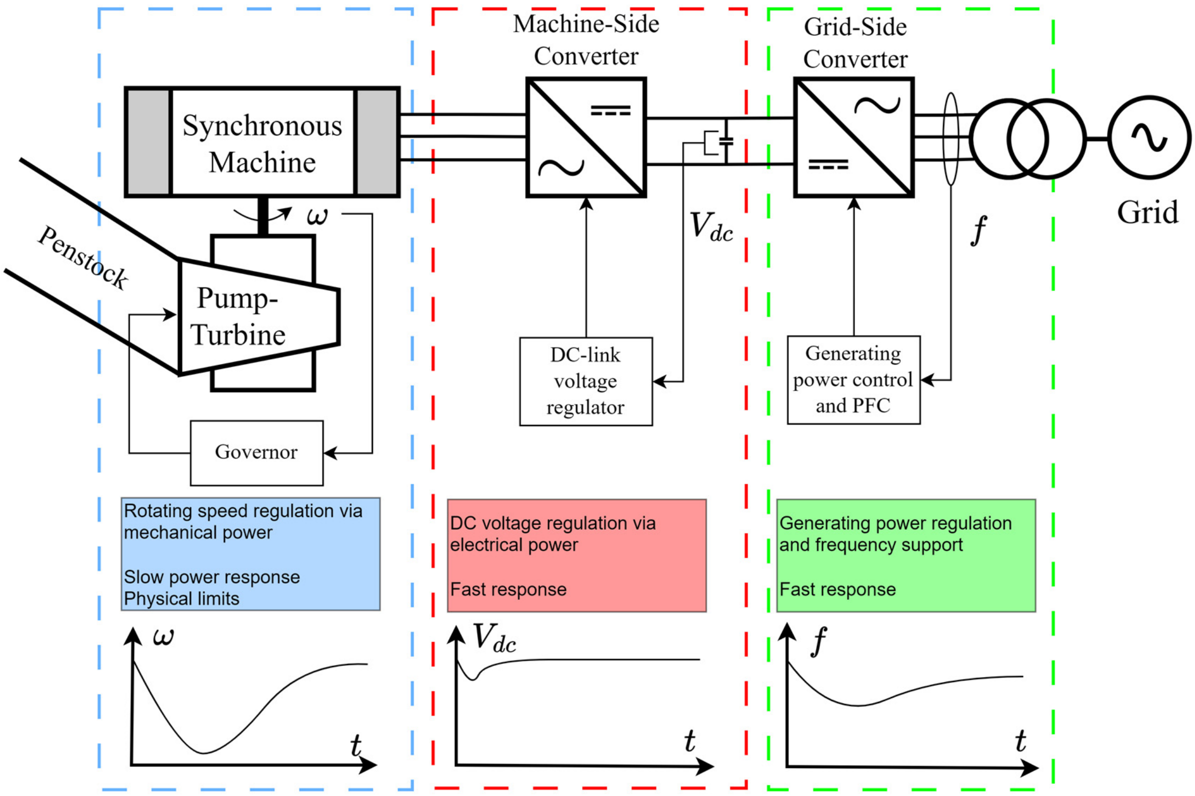


**Figure 1.** Control scheme and dynamic response timescale mismatch in a VS-PHS system during grid frequency support.

The problem of control timescale mismatch in VS-PHS is particularly pronounced in systems with slow hydraulic dynamics. Slow dynamics may arise from a long penstock with a large water starting time—typical of high hydraulic head PHS systems, a limited guide-vane rate imposed to avoid extreme pressure fluctuations, or a sluggish hydraulic servomotor. Although the DC link has the potential to provide rapid power support, it remains underutilised. Efforts to deliberately slow the DC-link voltage-control loop, in order to reduce the reliance on rotor kinetic energy extraction for power injection, inevitably reduce phase margin and can drive the system towards instability. This is indicative of a structural limitation with independent control loops. Typically, the DC-link storage element is a capacitor with relatively low storage capacity, which cannot be considered to be a significant standalone energy source. Expanding this intermediate DC-link buffer to a larger storage capacity, by including additional fast-acting electrical storage (e.g., supercapacitors or batteries), provides an opportunity to increase the extent to which this fast electrical buffer can be used during transients. Reported VS-PHS systems in the literature are typically based on proportional–integral (PI) controllers for regulating speed and DC-link voltage, but they lack the ability to coordinate multiple subsystems or enforce output constraints [10]. The inherent limitations of these decoupled, single-input single-output structures necessitate advanced control strategies capable of handling multiple inputs and multiple outputs in a constraint-aware manner.

Model predictive control (MPC) provides a systematic framework for effective handling of multivariable systems with output constraints. MPC controllers predict how a plant and its state variables will evolve over a finite horizon, calculate the control sequence optimally to minimise the desired cost function while satisfying constraint conditions, and apply the required moves to controllable plant inputs. This optimisation is repeated at each sampling period, based on updated measurements and predictions, with the controller enacting the immediate next control move only at each interval. These capabilities make MPC well suited for applications that require coordinated control of multiple interacting variables.

MPC has been investigated in power system studies as a coordination framework for managing multiple generating units under operational constraints. It has been proposed as a central energy-management layer for automatic generation control [11,12], coordinating secondary frequency control among hydro generators while respecting generator capacities, ramp rates, and tie-line limits [13]. MPC has also been studied to coordinate multiple small hydropower plants to improve power quality during load variations, with simulations reporting reductions in voltage distortion, unbalance, and frequency overshoot [14]. Furthermore, a centralised MPC for active frequency response has been developed to coordinate diverse resources across interconnected areas, enforce tie-line and unit constraints, and improve frequency nadir and settling compared with conventional schemes [15]. These studies mainly address large-scale coordination across wide areas and extended time horizons.

For energy coordination at the plant level and over tighter time intervals, MPC has been proposed to coordinate an energy-storage system with a thermal generator to improve overall plant performance [16,17]. An MPC layer around a virtual synchronous generator with energy storage has been designed to improve frequency and voltage dynamics in islanded microgrids, with simulations demonstrating smaller overshoot and reduced settling times compared to conventional control [18]. These works indicate the potential of MPC for local-level coordination of multiple energy subsystems, providing a conceptual basis for its application to VS-PHS plants.

The application of MPC has also been extended to individual hydropower plants. In [19,20], the MPC-based governor control for a conventional fixed-speed hydro unit improves disturbance rejection and avoids integral wind-up (the phenomenon of accumulating error after an actuator reaches its limit) in a linear single-input single-output setting. A laboratory implementation of MPC demonstrates reduced rise time and settling time compared to a PI control approach. MPC has also been used to operate fixed-speed and variable-speed hydro units for higher efficiency and improved response to scheduled power setpoint changes in both turbine and pump modes [10,21,22]. An adaptive MPC approach has been proposed to proactively control power output to provide primary frequency support for a VS-PHS unit based on doubly fed induction machine technology [23]. However, this MPC approach requires models, parameters, and current operating points of other generators and loads in order to predict system power imbalance, which is difficult to achieve in practice. In Refs [24–26], MPC schemes for variable-speed hydropower have been shown, via power system simulation studies, to be capable of providing fast frequency response. In these works, DC-link voltage dynamics are omitted, and the power delivered to the grid is optimised to respect internal operational limits. This approach may be inconsistent with standard system operation, where power support must strictly adhere to the committed droop coefficient rather than being adjusted in real time to protect local unit constraints.

Electricity grid codes generally mandate requirements for generating units participating in primary frequency control. PFC must follow a standard and reliable response, proportional to observed frequency deviation and within a desired timeframe [27]. This ensures predictable and auditable performance across generating units. For reliability, the initial response should be local, fast and not dependent upon communication of setpoints. Therefore, the plant should not be dependent upon models of other units or on wide-area grid data in order to determine its control action. In practice, the grid operator and the plant operator agree on a pre-determined suitable droop coefficient that provides sufficient grid support without exceeding the plant's operational limits. A participating generator or flexible load is in turn responsible for implementing appropriate control in order to meet the agreed response within physical plant constraints.

This paper presents an MPC approach for VS-PHS units based on full-size converters, enabling rapid frequency response while respecting internal operating constraints. Unlike existing MPC-based VS-PHS studies that either optimise the grid-side power response for frequency support or focus on scheduled operating point changes, the proposed method preserves the plant's committed PFC response and uses MPC for internal energy coordination. Power delivered to the grid is regulated through an active power control loop implementing a standard PFC approach at the grid-side converter. The MPC in turn manages internal variables, relying solely on measurements available behind the point of common coupling (PCC), to match power injection provided by the grid-side converter with energy supplied from the DC link, machine and hydraulic system. With this framework, the MPC controller replaces the conventional PI-based governor and DC-link voltage regulator. Its objective is to coordinate the internal energy flows while enforcing output and actuator constraints. With built-in knowledge of plant dynamics, the MPC allocates the required power extraction over the frequency disturbance period between the hydraulic system, the rotating mass of the turbine–machine set and the DC link, allowing the DC-link capacitors to share the transient burden with the rotor inertia. The MPC scheme enables a proactive guide-vane action, which raises the mechanical power of the slow hydraulic system earlier and reduces the reactive behaviour observed under PI control.

The contributions of this paper are as follows:

- A VS-PHS system using full-size converters is studied under primary frequency control. A slow hydraulic response with a long penstock is considered a representative case, and MPC is applied to ensure safe operation during fast power support commitments.

- An MPC formulation is proposed that preserves the committed grid power support, incorporates output constraints, enables the coordinated use of the two energy buffers (the DC link and the rotating mass), and provides a proactive hydraulic response.
- Simulation results show that extending DC-link energy storage allows the DC link to support fast frequency response and reduces dependence on kinetic energy while the mechanical power ramps up.

The remainder of this paper is structured as follows. Section 2 details the dynamic modelling of the VS-PHS plant and formulates the proposed MPC method. Section 3 evaluates the controller through simulation case studies: primary frequency performance and energy-sharing coordination against baseline PI control; robustness under plant-model mismatch and sensor noise; and system response under aggressive frequency droop, which examines the impact of expanding the DC-link storage on mitigating the effects of slow hydraulic dynamics. Finally, Section 4 concludes the paper.

## 2. Methodology

### *2.1. Plant Modelling*

A VS-PHS unit employing full-size voltage source converters (VSCs) is considered, as shown in Figure 2. The main components include a long penstock, a hydraulic turbine, a synchronous generator, power electronic converters, and a DC link. This configuration decouples the synchronous machine from the grid and enables flexible speed operation in both pumping and generating modes. While the control architecture is fundamentally symmetric for both modes [28], to maintain analytical clarity, this study focuses on turbine mode, where the synchronous machine operates as a generator. The machine-side converter (MSC) works as a rectifier, and the grid-side converter (GSC) functions as an inverter delivering power to the grid. The VS-PHS system is represented by an integrated nonlinear dynamic model, hereafter referred to as the plant, comprising hydraulic and electrical subsystems. The high-fidelity nonlinear model captures the essential dynamics required for accurate simulations.

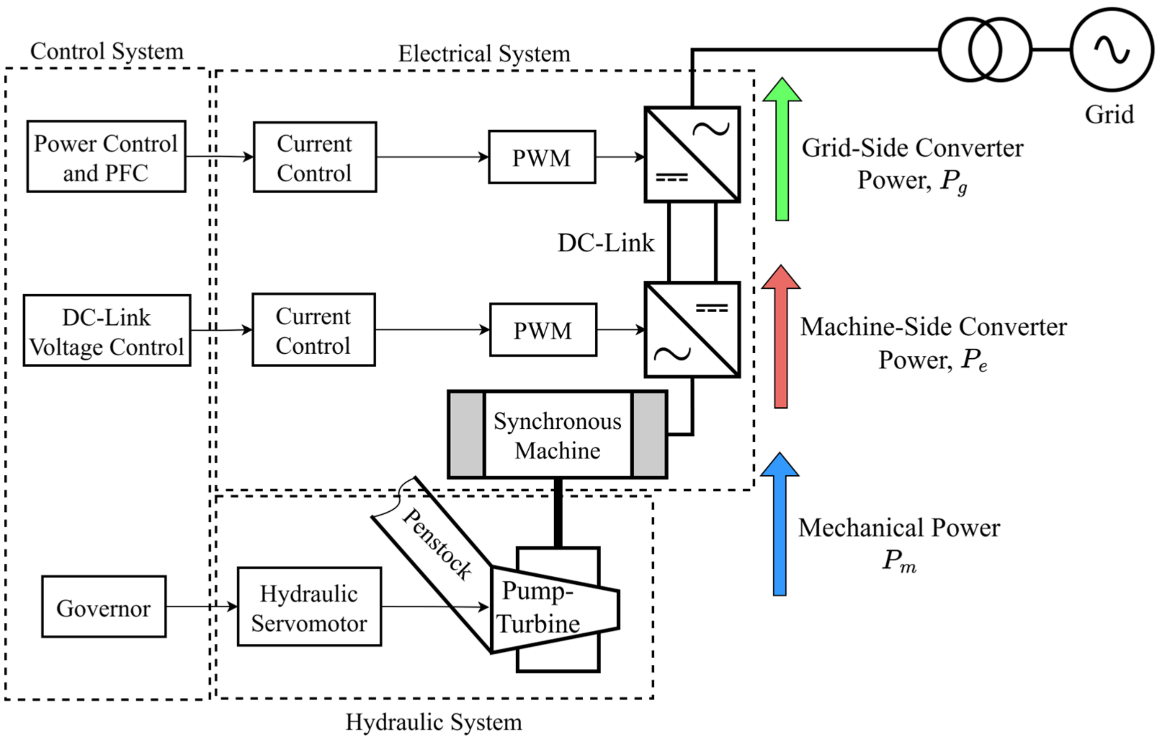


**Figure 2.** Configuration of the variable-speed pumped hydro storage unit using a full-size converter.

For control design, a linear model is derived by linearising the nonlinear system equations around a nominal steady-state operating point using small-signal analysis and neglecting higher-order terms. This linear representation serves as the basis for tuning PI controllers and for developing an MPC controller. Accordingly, each component of the plant is first described, followed by the corresponding linearised representation of each component being defined in detail.

### 2.1.1. Hydraulic System

The hydraulic system consists of the penstock, turbine and servomotor used for guide-vane positioning.

**Hydraulic Servomotor**

The servomotor is a hydraulic actuator that receives the reference guide-vane opening $G^*$ from the governor. The actual guide-vane opening $G$ regulates the flow $q$ into the pump-turbine, which in turn produces the mechanical power output. The servomotor dynamics are typically represented by a first-order transfer function [29] described by Equation (1):

$$\frac{G(s)}{G^*(s)} = \frac{1}{T_g s + 1} \tag{1}$$

where $T_g$ is the hydraulic servomotor time constant. This component is subject to physical constraints, including a ramp rate limit that restricts the guide-vane movement speed and position limits that define the limits of guide-vane opening. The servomotor is represented in block diagram form in Figure 3a.

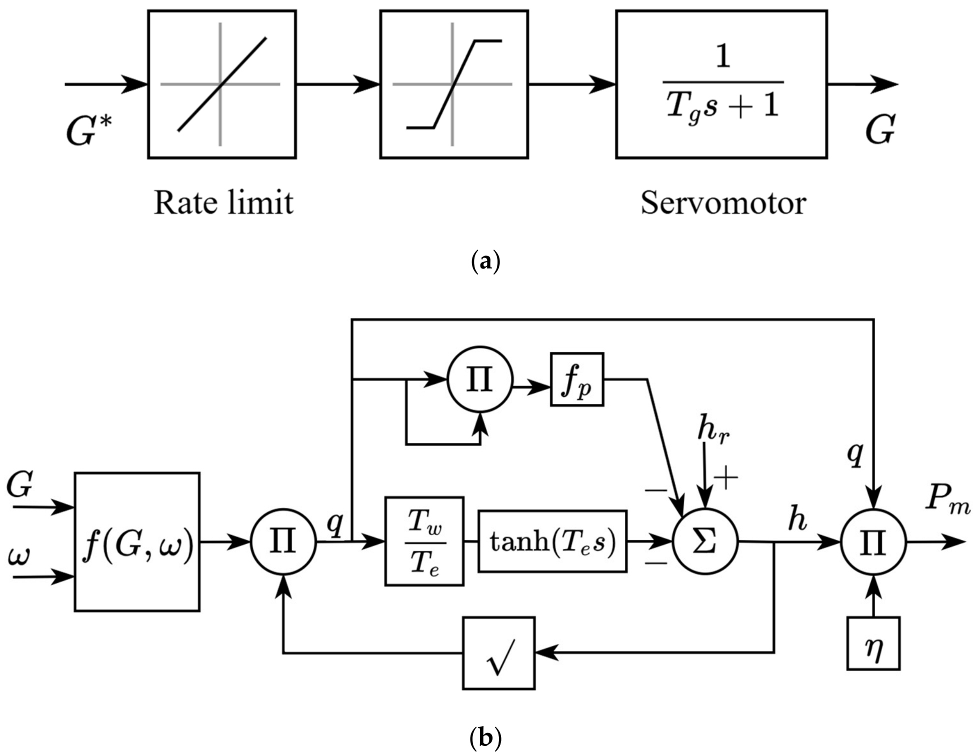


**Figure 3.** Hydraulic system block diagrams: (**a**) hydraulic servomotor; (**b**) penstock and turbine.

In state-space form, an internal state variable $g$ is introduced, and the transfer function in Equation (1) is expressed by Equations (2) and (3):

$$\dot{g} = A_g g + B_g G^* \tag{2}$$

$$G = C_g g + D_g G^* \tag{3}$$

The corresponding system matrices $A_g$, $B_g$, $C_g$, and $D_g$ are given in Appendix A.1.

**Penstock and Turbine**

The nonlinear model of the penstock with an elastic water column is used to capture the travelling-wave effects that occur in long waterways [29,30]. The relationship between turbine inlet head $h$ and the flow $q$ is given by Equation (4) [29]:

$$\frac{h(s)}{q(s)} = -\frac{T_w}{T_e}\tanh(T_e s) \tag{4}$$

where $T_w$ is known as the water starting time (or water inertia time constant), and $T_e$ is the wave travel time (or elastic time constant). As illustrated in Figure 3b, the turbine inlet head also includes frictional losses, which increase with the square of the flow, defined by the penstock friction coefficient $f_p$.

The turbine flow $q$ is a nonlinear function of the guide-vane opening $G$, the rotational speed $\omega$, and the turbine head $h$ [31], which is determined by turbine dimensions and the detailed design parameters of the turbine runner. At the rated head $h_r$, this relationship is described by a regression model $f\ (G, \omega)$, which is derived from extensive empirical data obtained from the turbine manufacturer, as detailed in [7]. The turbine flow, accounting for transient head variations, is obtained from the affinity law [32,33], as given by Equation (5):

$$q\ = f\ (G, \omega)\sqrt{\frac{h}{h_r}} \tag{5}$$

The corresponding mechanical power output from the turbine $P_m$ is a function of turbine flow, head and turbine efficiency $\eta$, as shown in Figure 3b. The mechanical power produced by the turbine drives the rotor of the synchronous generator.

A third-order state-space model is derived to approximate the plant dynamics between $G$ and $P_m$ around an operating point. Three internal state variables, $h_1$, $h_2$, and $h_3$, are introduced, with the state-space model being represented by Equations (6) and (7):

$$\dot{\begin{bmatrix} h_1 \\ h_2 \\ h_3 \end{bmatrix}} = A_h \begin{bmatrix} h_1 \\ h_2 \\ h_3 \end{bmatrix} + B_h G \tag{6}$$

$$P_m = C_h \begin{bmatrix} h_1 \\ h_2 \\ h_3 \end{bmatrix} + D_h G \tag{7}$$

where the state-space matrices $A_h$, $B_h$, $C_h$ and $D_h$ are as provided in Appendix A.2.

#### 2.1.2. Electrical System

The electrical system consists of the synchronous generator, the MSC, and the GSC, as illustrated in Figure 2. The synchronous generator converts mechanical power supplied by the turbine into electrical power. The GSC is operated to supply power to the grid to meet the desired export setpoint. The MSC, in turn, operates as a rectifier to regulate the DC-link voltage to ensure power exchange balance between the GSC and the MSC.

**Synchronous Generator**

The mechanical power produced by the turbine drives the synchronous generator rotor, which in combination with the machine's excitation system induces voltage across the stator windings. In converter-fed VS-PHS units, the stator is connected to a full-size AC/DC converter, referred to as the MSC, which controls electrical power $P_e$ to maintain charge at the DC-link capacitors. The DC-link voltage is discharged through the GSC, delivering AC power $P_g$ to the grid. The rotational speed deviation is therefore influenced by the power imbalance between the mechanical power $P_m$ and the electrical power $P_e$ drawn by the MSC. Rapid power extraction for grid frequency support can utilise the flywheel effect of the kinetic energy stored in the rotor.

The synchronous machine and its excitation system are represented by the IEEE standard high-fidelity models [34]. For speed governor design, only the rotational speed dynamics described by the swing equation are retained. The rotational speed deviation ($\Delta\omega$) is described in Equation (8):

$$2H_m \frac{d\Delta\omega}{dt} = P_m - P_e - D_m \Delta\omega \tag{8}$$

where $H_m$ is the machine inertia constant, and $D_m$ is the damping coefficient representing the mechanical damping effects. Defining the state variable $\Delta\omega$, the state-space representation of Equation (8) is expressed in Equations (9) and (10):

$$\Delta\dot{\omega} = A_\omega \Delta\omega + B_\omega \begin{bmatrix} P_m \\ P_e \end{bmatrix} \tag{9}$$

$$\Delta\omega = C_\omega \Delta\omega + D_\omega \begin{bmatrix} P_m \\ P_e \end{bmatrix} \tag{10}$$

where the system matrices $A_\omega$, $B_\omega$, $C_\omega$, and $D_\omega$ are as provided in Appendix A.3.

**Converters**

The converters regulate power flow between the generator, the DC link, and the grid. On the machine side, the MSC power $P_e$ is transferred to the DC link by controlling the generator current $I_m$. On the grid side, the GSC power $P_g$ is delivered to the grid by regulating the grid injection current $I_g$. Both converters are modelled as VSCs incorporating the standard $abc/dq$ transformations, current control loops, and pulse-width modulation (PWM) [35]. Synchronous reference frames are chosen for the converters such that the $d$-axis current dictates the active power. In this structure, the measured three-phase currents are transformed to the $dq$ frame and regulated by feedforward-decoupled current controllers. The resulting voltage references are transformed back to $abc$ quantities and applied to the PWM process.

The dynamics on the $d$-axis, which correspond to active power flow, are the focus of this section. The complete closed-loop response of the inner current controller, which encompasses the regulation, the physical system dynamics, and the converter PWM switching delays, is typically approximated by an equivalent first-order transfer function defined by Equations (11) and (12):

$$\frac{I_{md}(s)}{I_{md}^*(s)} = \frac{1}{T_c s + 1} \tag{11}$$

$$\frac{I_{gd}(s)}{I_{gd}^*(s)} = \frac{1}{T_c s + 1} \tag{12}$$

where $T_c$ is the effective current loop time constant, and the subscript $d$ denotes $d$-axis quantities. The effective current loop time constant $T_c$ represents the closed-loop bandwidth of this current control system. In practice, to ensure stability and avoid interference, the current controllers are tuned such that this bandwidth is at least one decade smaller than the converter switching frequency [35].

Defining the states $i_{md}$ and $i_{gd}$, the state-space representation of the current control loops is expressed in Equations (13) and (14):

$$\begin{bmatrix} \dot{i}_{md} \\ \dot{i}_{gd} \end{bmatrix} = A_c \begin{bmatrix} i_{md} \\ i_{gd} \end{bmatrix} + B_c \begin{bmatrix} I^*_{md} \\ I^*_{gd} \end{bmatrix} \tag{13}$$

$$\begin{bmatrix} I_{md} \\ I_{gd} \end{bmatrix} = C_c \begin{bmatrix} i_{md} \\ i_{gd} \end{bmatrix} + D_c \begin{bmatrix} I^*_{md} \\ I^*_{gd} \end{bmatrix} \tag{14}$$

where the corresponding system matrices $A_c$, $B_c$, $C_c$, and $D_c$ are as provided in Appendix A.4.

The DC link acts as the intermediate energy buffer between the MSC and GSC, and its voltage reflects the instantaneous balance between the electrical power drawn from the generator and the power delivered to the grid. A linear model of the DC-link voltage dynamics, based on the charging and discharging currents of the DC-link capacitors, can be expressed as in Equation (15):

$$C_{dc}\frac{dV_{dc}}{dt} = \frac{P_e - P_g}{V_{dc}} - \frac{V_{dc}}{R_{dc}} \tag{15}$$

where $C_{dc}$ is the equivalent DC-link capacitance and $R_{dc}$ represents the equivalent leakage resistance. While leakage resistance results in insignificant self-discharge over the timescale of relevant dynamic events, a high-value shunt resistance is included in the DC-link dynamics to improve the numerical conditioning of the state-space realisation (the state matrix is non-zero).

The converter powers expressed in per-unit form are shown in Equations (16) and (17):

$$P_e = V_{md}I_{md} + V_{mq}I_{mq} \tag{16}$$

$$P_g = V_{gd}I_{gd} + V_{gq}I_{gq} \tag{17}$$

where $V_{md}$ and $V_{gd}$ are the $d$-axis voltages of the synchronous machine and the grid, respectively; $V_{mq}$ and $V_{gq}$ are the corresponding $q$-axis voltages. By aligning the $abc/dq$ synchronous reference frames with the respective machine and grid voltages, the $q$-axis voltages are forced to zero, which simplifies the active power equations to depend solely on the $d$-axis component. Substituting these expressions into Equation (15) yields the nonlinear voltage dynamics as in Equation (18):

$$C_{dc}\frac{dV_{dc}}{dt} = \frac{V_{md}}{V_{dc}}I_{md} - \frac{V_{gd}}{V_{dc}}I_{gd} - \frac{V_{dc}}{R_{dc}} \tag{18}$$

Linearising Equation (18) around a steady-state operating point and neglecting higher-order terms gives the small-signal model in Equation (19):

$$C_{dc}\frac{d(\Delta V_{dc})}{dt} = K\left(\Delta I_{md} - \Delta I_{gd}\right) - \frac{1}{R_{dc}}\Delta V_{dc} \tag{19}$$

where $K = V_{md}/V_{dc} \approx V_{gd}/V_{dc}$ is treated as constant under normal operating conditions. The corresponding transfer function of the linear model is expressed in Equation (20):

$$\Delta V_{dc}(s) = \left[\Delta I_{md}(s) - \Delta I_{gd}(s)\right]\frac{K}{C_{dc}s + 1/R_{dc}} \tag{20}$$

For the state-space representation, defining a state as $v_{dc}$, the linear dynamic model shown in Equation (20) is expressed in Equations (21) and (22):

$$\dot{v_{dc}} = A_v v_{dc} + B_v \begin{bmatrix} I_{md} \\ I_{gd} \end{bmatrix} \tag{21}$$

$$V_{dc} = C_v v_{dc} + D_v \begin{bmatrix} I_{md} \\ I_{gd} \end{bmatrix} \tag{22}$$

The system matrices $A_v$, $B_v$, $C_v$, and $D_v$ are provided in Appendix A.5.

### *2.2. Control System—PI Based*

The conventional approach for power flow control in VS-PHS is to employ independent control of GSC, MSC and turbine governor, using PI control [28]; in this study we follow this approach to provide a benchmark to enable comparison with our proposed MPC approach. The PI control structure follows a hierarchical arrangement, as shown in Figure 4, where the 'Governor', 'DC-link voltage control' and 'Active power control' blocks each represent tuned PI controllers; in this figure we also indicate where conventional control blocks are replaced by the proposed MPC. At the highest level, the hydraulic governor, the MSC's DC-link voltage control, and the GSC's active power control dictate the active power flow through the turbine, the synchronous generator, the DC link, and the grid. At the lower level, the current control loops, PWM, and the associated *abc*/*dq* transformations, introduced in the converter model descriptions, are treated as part of the plant.

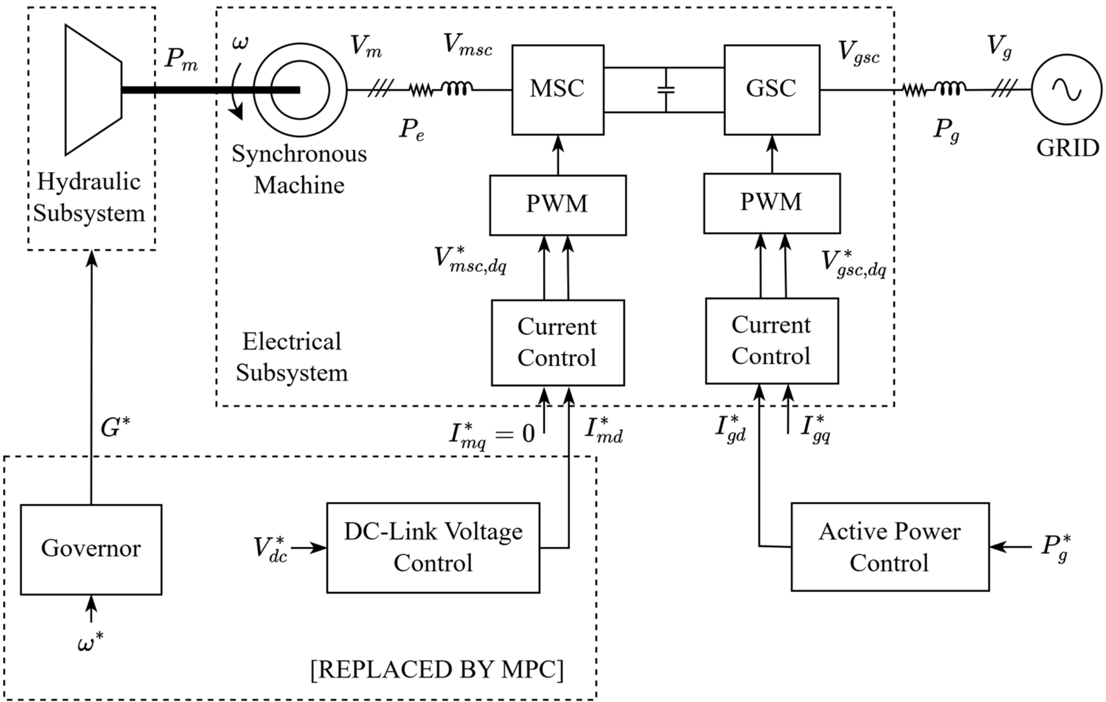


**Figure 4.** Control loops of the system focusing on active power flow.

Figure 5 shows the block diagram of the GSC active power control. The power setpoint $P_{set}$ is commanded by the grid operator, while the droop coefficient $R_p$ determines the additional required power contribution owing to any frequency deviations such as might occur during a power system contingency event. The measured grid-side power $P_g$ is compared with this combined reference value, with the resulting power error fed through a PI controller to generate the $d$-axis current reference $I^*_{gd}$, which the inner current control loop subsequently tracks.

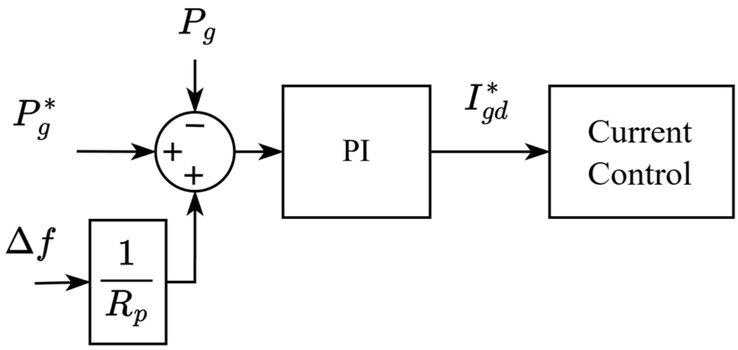


**Figure 5.** Block diagram of the GSC's active power control.

In Figure 6a, the DC-link voltage $V_{dc}$ is regulated by a PI controller that generates the $d$-axis current reference $I^*_{md}$, which is tracked by the inner current control loop. The resulting current $I_{md}$ charges the DC-link capacitors, thereby regulating the DC-link voltage. Figure 6b shows the governor, where the rotational speed error is processed by a PI controller to generate the guide-vane position reference $G^*$. The servomotor adjusts guide-vane opening $G$ accordingly, thus affecting the turbine flow and mechanical power $P_m$, which in turn influences the rotational speed dynamics. The linear models introduced earlier are used to tune the PI controllers.

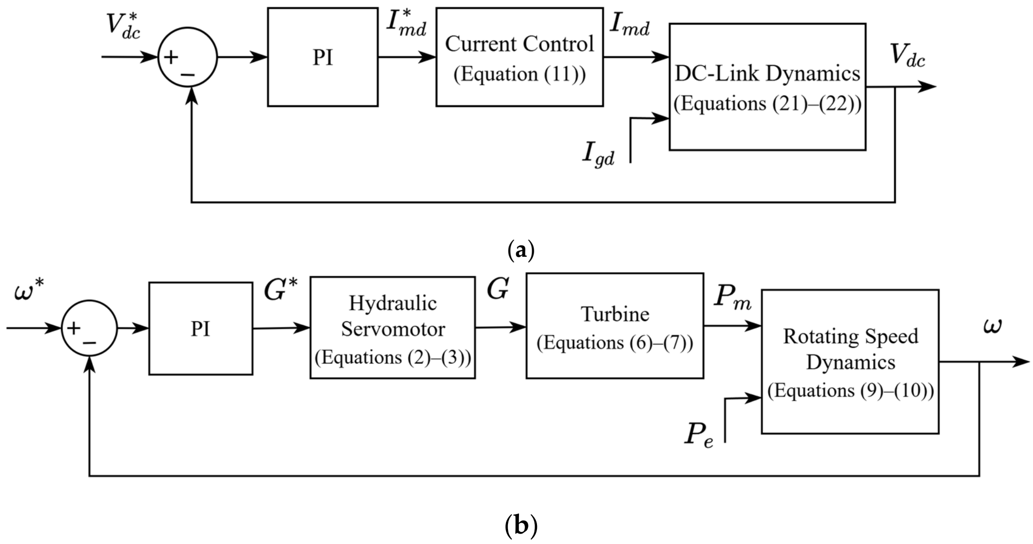


**Figure 6.** Control loops designed using linear models for tuning: (**a**) DC-link voltage regulation; (**b**) governor speed control.

### *2.3. Proposed Model Predictive Control Method*

In the proposed control approach, MPC replaces the governor and DC-link voltage control in the control hierarchy (Figure 4). In this configuration, the MPC directly commands the guide-vane reference $G^*$ and the machine-side $d$-axis current reference $I^*_{md}$, such that they are no longer treated as decoupled subsystems to be independently controlled. The GSC active-power control remains outside the MPC system, allowing it to continue operating under standard droop control. Under this arrangement, the grid-side current reference ($I^*_{gd}$) appears to the MPC as a plant input disturbance which acts on the DC-link dynamics.

The purpose of the MPC is to coordinate the internal energy flows of the VS-PHS unit while enforcing constraints on the hydraulic actuator, the electrical currents, the rotational speed deviation, and the DC-link voltage. Unlike PI control, which treats the hydraulic and electrical loops independently, MPC uses a prediction model of the coupled system to allocate energy between the rotating mass, the DC link, and the hydraulic input in a constraint-aware manner. This allows the controller to respond proactively to speed and voltage deviations, expanding the usable energy of the DC link during fast power changes and reducing excessive reliance on rotor kinetic energy, while respecting the actuator and output constraints.

Figure 7 summarises the closed-loop MPC architecture. Here, $x_k$ collects the servo, hydraulic, electrical, and DC-link states; $u_k$ contains the control inputs commanded by MPC; $y_k$ contains the measured outputs. Additionally, $r_k$ represents the reference trajectory vector, and $d_k$ represents the disturbance state vector. At each discrete time step, the MPC module uses the state and disturbance estimates ($\hat{x}_k$ and $\hat{d}_k$) from the estimator to predict future plant behaviour, solve the constrained optimisation problem, and generate the optimal control inputs, which are applied to the nonlinear plant.

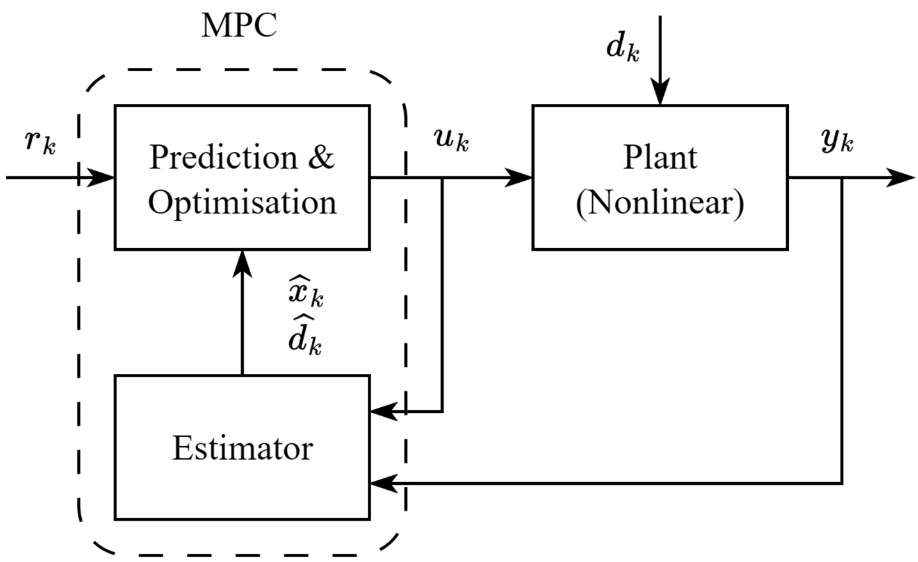


**Figure 7.** Overall MPC system structure, illustrating the closed-loop interaction between the predictive controller, the state estimator, and the nonlinear physical plant.

2.3.1. Prediction Model and Estimator

For MPC design, a linear prediction model is constructed by combining the linear models of the components that are presented in previous subsections, as illustrated in Figure 8. The resulting continuous-time state-space model is discretised with the sampling period $T_s$, equal to the MPC step [36]. The discrete state-space representation serving as the prediction model is given by Equations (23) and (24):

$$x_{k+1} = Ax_k + Bu_k \tag{23}$$

$$y_k = Cx_k \tag{24}$$

where

- $x_k = \left[g, h_1, h_2, h_3, \Delta\omega, i_{md}, v_{dc}, i_{gd}\right]^T$ is the model state vector;
- $u_k = [G^*, I^*_{md}]^T$ is the control input vector by the MPC;
- $y_k = [G, P_m, \Delta\omega, I_{md}, V_{dc}]^T$ is the measured output vector;
- $A \in \mathbb{R}^{8\times 8}$, $B \in \mathbb{R}^{8\times 2}$, and $C \in \mathbb{R}^{5\times 8}$ are system matrices, provided in Appendix A.6.

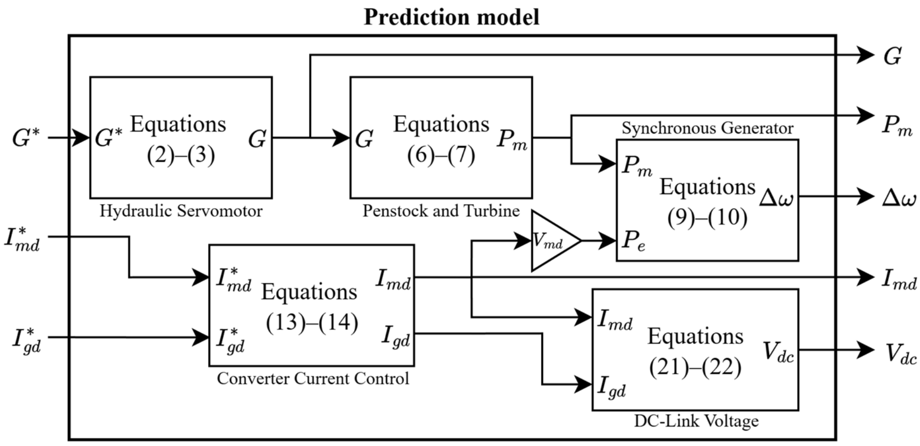


**Figure 8.** Construction of the prediction model.

In this MPC formulation, the grid-side current reference ($I^*_{gd}$) is excluded, since it is generated independently by the GSC active power control loop according to standard PFC principles. In accordance with grid-code requirements, this droop action must remain predictable and auditable [37], and hence the MPC is arranged to preserve this functionality. As a result, all GSC-related current dynamics appear to the MPC as a persistent disturbance acting on the DC-link voltage. For example, when $I^*_{gd}$ changes following a frequency variation, the MPC observes this as a random step-like disturbance acting on the $V_{dc}$.

Furthermore, the linear prediction model cannot natively account for plant-model mismatch caused by inherent system nonlinearities and unmodelled dynamics. Without correction, constant biases will emerge between the model predictions and the actual plant [38]. Specifically, in this system, the inherently nonlinear hydraulic and DC-link voltage dynamics are linearised around a single nominal working point. When the system deviates from this point during severe transients, the linear prediction model loses accuracy, resulting in biases on both the rotational speed deviation $\Delta\omega$ and DC-link voltage $V_{dc}$.

For offset-free tracking of the DC-link voltage and rotational speed, the prediction model is augmented with an integrating disturbance state vector ($d_k$) driven by white-noise sequences ($w_k$). This vector contains two integrating states that accumulate the respective biases caused by the input disturbance from $I^*_{gd}$ and the output disturbance from the model mismatch. By augmenting the linear model with this disturbance state vector, the MPC can continually adjust the control inputs to compensate for the lumped effects of model error and persistent disturbances [38,39]. The disturbance-augmented model is introduced in Equations (25) and (26) [38]:

$$\begin{bmatrix} x_{k+1} \\ d_{k+1} \end{bmatrix} = \begin{bmatrix} A & B_d \\ 0 & I \end{bmatrix} \begin{bmatrix} x_k \\ d_k \end{bmatrix} + \begin{bmatrix} B \\ 0 \end{bmatrix} u_k + w_k \tag{25}$$

$$y_k = [C C_d] \begin{bmatrix} x_k \\ d_k \end{bmatrix} + v_k \tag{26}$$

where

- $d_k \in \mathbb{R}^{2\times1}$ represents the disturbance state vector;
- $B_d \in \mathbb{R}^{8\times2}$ and $C_d \in \mathbb{R}^{5\times2}$ map the disturbances to the model states and the measured outputs, respectively;
- $I \in \mathbb{R}^{2\times2}$ is the identity matrix, corresponding to the two integrating disturbance states;
- $w_k \in \mathbb{R}^{10\times1}$ and $v_k \in \mathbb{R}^{5\times1}$ represent zero-mean uncorrelated process noise and measurement noise sequences affecting the augmented states and measured outputs, respectively.

Following the offset-free MPC formulation, two integrating disturbance states are introduced. Incorporating these states into the formulation ensures the controller is able to provide offset-free tracking for two controlled outputs [38]: rotational speed deviation and DC-link voltage. With the two sources of bias described above, the matrices $B_d$ and $C_d$ are specifically structured to map these distinct disturbance channels into the prediction model. The matrix $B_d$ routes the first disturbance channel into the relevant electrical states to capture the persistent integrating effect on the DC-link voltage. Conversely, $C_d$ routes the second disturbance channel directly to the rotational speed deviation. Matrices $B_d$ and $C_d$ are given in Appendix A.6.

The augmented states in the system described by Equations (25) and (26) are not directly measurable and must be estimated from the plant's inputs and outputs. A Kalman-based state estimator is designed to estimate both the physical state $x_k$ and the disturbance state $d_k$. The correction step is given by Equation (27) [38]:

$$\begin{bmatrix} \hat{x}_{k|k} \\ \hat{d}_{k|k} \end{bmatrix} = \begin{bmatrix} \hat{x}_{k|k-1} \\ \hat{d}_{k|k-1} \end{bmatrix} + M\left( y_k - [C\ C_d] \begin{bmatrix} \hat{x}_{k|k-1} \\ \hat{d}_{k|k-1} \end{bmatrix} \right) \tag{27}$$

where

- $M \in \mathbb{R}^{10\times 5}$ is the estimator gain for the augmented states.
- $\hat{x}_{k|k-1}$, $\hat{d}_{k|k-1}$ are the states predicted at time $k-1$ for step $k$.
- $\hat{x}_{k|k}$, $\hat{d}_{k|k}$ are the corrected estimations at time $k$, which are $\hat{x}_k$, $\hat{d}_k$.

At each time step $k$, given the measurements $y_k$, the estimator corrects the estimated states from the state prediction and the error (difference between measured and predicted output) according to Equation (27). By assuming the fundamental stochastic noise sources ($w_k$ and $v_k$) are independent with unit variance, the process noise and measurement noise covariance matrices can be systematically determined. The optimal estimator gain matrix $M$ is then computed offline by solving the discrete-time algebraic Riccati equation, given in Appendix A.7.

From Equations (25)–(27), the prediction step, used to propagate the states forward, is determined by Equations (28) and (29) [38]:

$$\begin{bmatrix} \hat{x}_{k+1|k} \\ \hat{d}_{k+1|k} \end{bmatrix} = \begin{bmatrix} A & B_d \\ 0 & I \end{bmatrix} \begin{bmatrix} \hat{x}_{k|k} \\ \hat{d}_{k|k} \end{bmatrix} + \begin{bmatrix} B \\ 0 \end{bmatrix} u_k \tag{28}$$

$$\hat{y}_{k+1|k} = [C\ C_d] \begin{bmatrix} \hat{x}_{k+1|k} \\ \hat{d}_{k+1|k} \end{bmatrix} \tag{29}$$

At each sampling instant, the predicted state $\left[\hat{x}_{k+1|k}, \hat{d}_{k+1|k}\right]^T$ from Equations (28) and (29) serves as the prior estimate and is updated by the correction step in Equation (27) in the following step. The MPC controller then uses these estimations to adjust the control inputs, compensating for model mismatch and persistent unmeasured disturbances. As a result, the predicted and actual plant outputs converge to their desired setpoints [39].

### 2.3.2. Receding Horizons Prediction

The MPC controller uses the updated state estimate ($\hat{x}_k$, $\hat{d}_k$) to predict system behaviour over a finite prediction horizon ($N_p$). By repeating the recursion in Equations (28) and (29), the augmented state and output trajectories are propagated forward for $i = 1, \ldots, N_p$ [39] as shown in Equations (30) and (31):

$$\begin{bmatrix} \hat{x}_{k+i|k} \\ \hat{d}_{k+i|k} \end{bmatrix} = \begin{bmatrix} A & B_d \\ 0 & I \end{bmatrix} \begin{bmatrix} \hat{x}_{k+i-1|k} \\ \hat{d}_{k+i-1|k} \end{bmatrix} + \begin{bmatrix} B \\ 0 \end{bmatrix} u_{k+i-1} \tag{30}$$

$$\hat{y}_{k+i|k} = [C\ C_d] \begin{bmatrix} \hat{x}_{k+i|k} \\ \hat{d}_{k+i|k} \end{bmatrix} \tag{31}$$

where $u_{k+i-1}$ is the input scheduled for time $k+i-1$. The Equations (30) and (31) reflect causality, in that the predicted state at time $k+i$ depends on the input scheduled for time $k+i-1$. During optimisation, the MPC computes the sequence of future control inputs $u_k, u_{k+1}, \ldots, u_{k+N_c-1}$, where $N_c$ denotes the control horizon and typically $N_c < N_p$. In implementation, only the immediate next control action is taken at each MPC step, with the complete sequence of control inputs re-computed for the entire horizon at every step. For steps beyond the control horizon, the scheduled input is held constant [40], given by Equation (32):

$$u_{k+i} = u_{k+N_c-1}, \text{with } i = N_c, \ldots, N_p - 1 \tag{32}$$

These predicted trajectories form the basis of the optimisation problem introduced in the next subsection.

#### 2.3.3. Control Objectives and Optimisation Problem

The primary control objective is to track the rotational speed deviation and the DC-link voltage to their references while preventing these outputs from exceeding any imposed limits during transient operation. A key strength of MPC is the ability to impose explicit constraints on both the control inputs and the plant outputs. Two types of constraints are considered in this plant:

1. Hard constraints of control inputs, which cannot be violated, reflecting the physical limits of the guide vane and current capabilities of the MSC:
   - Input limits: guide-vane position $G_{\min} \leq G^* \leq G_{\max}$, and MSC current $I_{md,\min} \leq I^*_{md} \leq I_{md,\max}$.
   - Input rate limits: maximum rate of change of $G^*$ ($R_{G,\max}$) and maximum rate of change of $I^*_{md}$ ($R_{I,\max}$).
2. Soft constraints of the plant outputs; these should be maintained but are allowed to be violated at a cost:
   - Rotational speed deviation: $\Delta\omega_{\min} \leq \Delta\omega \leq \Delta\omega_{\max}$.
   - DC-link voltage: $V_{dc,\min} \leq V_{dc} \leq V_{dc,\max}$.

The specified limits for rotational speed deviation and DC-link voltage are necessary for safe and reliable operation. Restricting deep rotational speed deviations helps maintain operation within an acceptable speed region, avoiding operation associated with cavitation and hydraulic instability risk [8]. Furthermore, maintaining rotational speed within prescribed bounds is critical for stable voltage regulation by the generator's excitation system, ensuring consistent electrical output. The DC-link voltage must remain within its limits to guarantee stable commutation of the converters. In the current formulation, we use rotational speed and DC-link voltage as the key soft constraints. It should be noted that the MPC optimisation can be formulated to include other plant quantities, such as rotor acceleration, turbine shaft differential torque, or penstock hydraulic pressure, provided suitable models are incorporated into the MPC prediction model.

These output constraints are implemented as soft constraints via the introduction of a non-negative slack variable $\varepsilon_k$, permitting limited violations when necessary:

$$\Delta\omega_{\min} - \varepsilon_k \leq \Delta\omega \leq \Delta\omega_{\max} + \varepsilon_k \tag{33}$$

$$V_{dc,\min} - \varepsilon_k \leq V_{dc} \leq V_{dc,\max} + \varepsilon_k \tag{34}$$

The optimisation cost function is then formulated to incorporate plant output tracking, smooth control input behaviour, and soft-constraint violation as defined in Equation (35):

$$J = \sum_{i=1}^{N_p} \left( r_{k+i} - \hat{y}_{k+i|k} \right)^T W_y^2 \left( r_{k+i} - \hat{y}_{k+i|k} \right) + \sum_{i=0}^{N_c-1} \Delta u_{k+i|k}^T W_\Delta^2 \Delta u_{k+i|k} + \rho^2 \varepsilon_k^2 \tag{35}$$

subject to the constraints:

$$\begin{gathered} G_{\min} \leq G^* \leq G_{\max} \\ I_{md,\min} \leq I_{md}^* \leq I_{md,\max} \\ -R_{G,\max} T_s \leq \Delta G^* \leq R_{G,\max} T_s \\ -R_{I,\max} T_s \leq \Delta I_{md}^* \leq R_{I,\max} T_s \\ \Delta\omega_{\min} - \varepsilon_k \leq \Delta\omega \leq \Delta\omega_{\max} + \varepsilon_k \\ V_{dc,\min} - \varepsilon_k \leq V_{dc} \leq V_{dc,\max} + \varepsilon_k \end{gathered}$$

where

- $r_{k+i}$ contains the output references;
- $\Delta u_{k+i|k} = u_{k+i|k} - u_{k+i-1|k}$ are the input increments;
- $\varepsilon_k$ is the slack variable;
- $W_y$ contains the output tracking weights;
- $W_\Delta$ contains the control input rate weights;
- $\rho$ is the weight penalising soft-constraint violations.

The first term in $J$ penalises deviations of predicted outputs from their references over the prediction horizon, ensuring that $\Delta\omega$ and $V_{dc}$ track their references. The second term penalises large input increments, promoting smooth actuator behaviour of $G^*$ and $I_{md}^*$. The third term penalises violations of the soft constraints, which are required to preserve feasibility under severe disturbances. In practice, when a severe disturbance occurs and it becomes physically impossible to keep the outputs within strict boundaries, treating those boundaries as unbreakable hard limits would lead to an infeasible optimisation problem. Adding the slack variable as in Equations (33) and (34) mathematically expands the boundary limits just enough to find a feasible solution. By heavily penalising the violation with the weight $\rho$, the optimisation strategically dictates control moves that push the system back inside the original boundaries, returning the slack to zero.

It should be noted that in this paper, the controlled outputs have equal boundary relaxations. A more general approach to implement soft constraints can be alternatively applied by introducing multiple independent non-negative slack variables for every constraint, which are subsequently individually penalised in the cost function [40]. Alternatively, a slack variable can be scaled to account for variables with different physical units or strictness levels [41].

The cost function in (35), together with the prediction model (30)–(31) and the input constraints, defines an optimisation problem. By expressing the predicted output trajectory over the horizon in lifted form, the objective function becomes a quadratic function of the future control increments, and the constraints take an affine form. This results in a standard quadratic program (QP). Given $W_{\Delta}^2 \succ 0$ and $\rho^2 > 0$, the QP is strictly convex and therefore admits a unique optimal solution at each sampling instant [40]. The MATLAB MPC Toolbox (version 2024b) is used to automatically construct the prediction, enforce the constraints, and compute the optimal control action using its built-in active-set QP solver [41].

### *2.4. Simulation Model Description*

The MPC framework proposed above can in principle be adapted to different VS-PHS systems. In this study, its coordination capabilities are best demonstrated under challenging operational conditions. A detailed nonlinear dynamic model representing a VS-PHS unit is utilised as the test plant. The parameters of the plant under study are detailed in Tables 1 and 2. The parameters defining the conventional baseline PI controllers are provided in Table 3, while the exact constraints and weighting matrices governing the proposed MPC are summarised in Table 4.

**Table 1.** Hydraulic subsystem parameters.

| Parameters | Values |
|---|---|
| Servomotor time constant, $T_g$ | 0.1 s |
| Maximum guide-vane rate limit, $R_{G,\max}$ | 0.05 pu/s |
| Water starting time, $T_w$ | 4 s |
| Wave travel time, $T_e$ | 1 s |
| Head loss coefficient, $f_p$ | 0.0052 |
| Rated hydraulic power | 100 MW |
| Turbine efficiency, $\eta$ | 92% |

**Table 2.** Electrical subsystem parameters.

| Parameters | Values |
|---|---|
| Synchronous generator | |
| Rated power | 100 MVA |
| Rated voltage | 13.8 kV |
| Inertia constant, $H_m$ | 3.5 s |
| Damping coefficient, $D_m$ | 0.5 |
| Converters | |
| Rated power | 100 MVA |
| AC rated voltage | 13.8 kV |
| DC-link rated voltage | 33 kV |
| Equivalent DC-link capacitance, $C_{dc}$ | 0.225 F |
| DC-link self-discharging resistance, $R_{dc}$ | 10 kΩ |
| Time constant of current control loops, $T_c$ | 0.01 s |

**Table 3.** PI control parameters.

| Parameters | Values |
|---|---|
| Governor PI coefficients | 0.8589, 0.0409 |
| DC-link voltage controller PI coefficients | 1.5192, 1.0060 |
| GSC power controller PI coefficients | 1, 4 |
| Droop control coefficient, $R_p$ | 0.04 |

**Table 4.** MPC settings, constraints and weighting parameters.

| Parameters | Values |
|---|---|
| Input Constraints | |
| Guide-vane position limits, $[G_{\min}, G_{\max}]$ | [0, 1] pu |
| Maximum guide-vane opening rate, $R_{G,\max}$ | 0.05 pu/s |
| MSC current limits, $[I_{md,\min}, I_{md,\max}]$ | [0, 1] pu |
| Maximum MSC current rate, $R_{I,\max}$ | 0.1 pu/s |
| Output Constraints | |
| Speed deviation limits, $[\Delta\omega_{\min}, \Delta\omega_{\max}]$ | [−0.15, 0.15] pu |
| DC-link voltage limits, $[V_{dc,\min}, V_{dc,\max}]$ | [0.9, 1.1] pu |
| Weights | |
| Control input rate weight matrix, $W_{\Delta}$ | diag(2000, 800) |
| Output tracking weight matrix, $W_y$ | diag(0, 0, 200, 0, 100) |
| Slack variable weight, $\rho$ | 5000 |
| MPC sampling time and horizons | |
| MPC sampling time, $T_s$ | 0.05 s |
| MPC prediction horizon, $N_p$ | 200 steps |
| MPC control horizon, $N_c$ | 30 steps |

The independent PI controllers were tuned using the linearised models as introduced in Figure 6. The tuning process is fundamentally balancing a trade-off between speed (indicated by the bandwidth, i.e., gain crossover frequency) and robustness (indicated by the phase and gain margins). Pushing the bandwidth higher yields a faster dynamic response but inevitably degrades the phase margin, making the system vulnerable to large disturbances and nonlinear plant variations. Therefore, the tuning objective for the baseline PI controllers was to achieve good bandwidths with safe margins.

For the hydraulic governor loop (Figure 6b), frequency response analysis of the tuned controller, given in Table 3, yields a bandwidth of 0.12 rad/s with a phase margin of 45.6° and a gain margin of 10.6 dB. The margins are within the recommended practice of a governor of a hydro unit [42]. The pumped hydro plant features a long penstock, which introduces a large water starting time. Consequently, if the gains are increased in an attempt to accelerate mechanical power response (e.g., to 0.24 rad/s), the gain and phase margins eventually drop below 5 dB and 30°. This degradation increases the risk of instability during large hydraulic transients.

For the DC-link voltage controller, the tuned parameters yield a bandwidth of 1.15 rad/s with a phase margin of 59.5°. This bandwidth is significantly faster than the mechanical hydraulic loop (0.12 rad/s). Attempting to deliberately lower this bandwidth to reduce the reliance on rotor kinetic energy extraction and relieve transient stress on the rotational speed only marginally reduces the bandwidth to 0.89 rad/s, offering no meaningful timescale improvement. More importantly, this reduction degrades the phase margin to 33.5°. Physically, pushing the bandwidth any lower severely reduces the phase margin and exposes the system to a high risk of instability.

The MPC parameters are provided in Table 4. The sampling time of 0.05 s is selected to capture the electrical dynamics while allowing the inner current control loops to settle within each MPC sampling interval. The prediction horizon of 200 steps provides a 10 s look-ahead, covering the slow dynamics. The control horizon of 30 steps limits the number of optimisation variables, lowering the computational burden. Additionally, the weights in the cost function dynamically shift the controller's behaviour based on the transient severity. Near steady state, the heavy input-rate penalties contribute to the total, which is relatively large compared to the output-tracking penalties. This discourages large control forces for minor variations. In contrast, during large variations of the tracking outputs, the sum of the tracking errors over the 200-step horizon is substantially higher than the rate penalties, driving the MPC to take aggressive corrective action. Finally, the very high soft-constraint weight strongly discourages any excursion outside the boundaries of the soft constraints, forcing the controller to sacrifice smooth operation to pull the variables back into the safe bounds.

## 3. Simulations and Results

Simulation studies have been conducted for the nonlinear VS-PHS plant model described in preceding sections, using both PI and MPC control. Since PHS plants in power systems are primarily designed for large energy storage capacities per unit of water volume stored, they usually feature hydraulic systems where upper and lower reservoirs are separated by a large vertical distance, thus being characterised as systems with large head and long penstocks [2]. Such systems can be characterised by large water-starting times and correspondingly slow hydraulic response [43,44]. Hence, the focus of case studies in this work is on investigating fast response capabilities of VS-PHS systems featuring large water starting times. In order to evaluate the performance of the PHS system in providing primary frequency response, simulations are conducted under a contingency event scenario which sees a significant frequency excursion. The simulated disturbance sees an active power imbalance which results in a system-wide frequency excursion of over 0.3 Hz. The dynamic response of the VS-PHS to the grid frequency disturbance is then investigated in detail.

### 3.1. Performance of MPC vs. PI Control

The VS-PHS system response using the proposed MPC is first compared with the response of conventionally tuned PI controllers under an identical frequency event. A power imbalance contingency creates a grid frequency deviation as shown in Figure 9a. The GSC responds by increasing its power output to support the grid, as shown in Figure 9b. The GSC power response is identical for both MPC and PI control methods, since the GSC power control loop operates independently and is governed by the external droop mechanism imposed by the grid operator. The relevant differences between the MPC and PI methods therefore appear in the internal dynamics. The constraints used in this study, corresponding to the MPC formulation defined earlier, are a ±15% soft bound on the rotational speed and a ±10% soft bound on the DC-link voltage. Short-term minor violations are permitted but are penalised via the cost function. Actuation is constrained by hard physical limits defined by a guide-vane rate of 0.05 pu/s and a converter current ramp of 0.1 pu/s. Performance is compared in terms of the resulting deviations in the rotational speed and DC-link voltage.

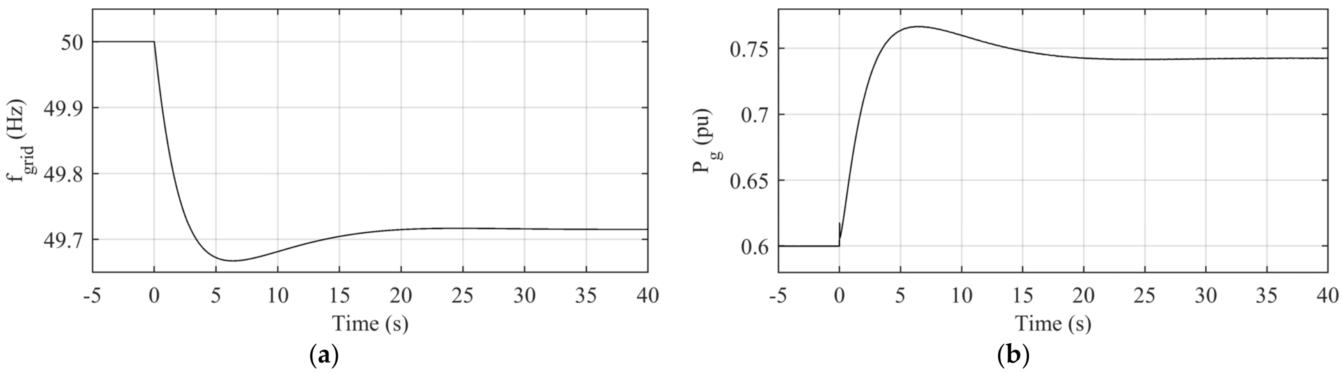


**Figure 9.** (**a**) Grid frequency, $f_{grid}$, during a power imbalance event, and (**b**) the corresponding droop control response of the grid-side converter, $P_g$.

Figure 10a shows how PI control prioritises holding the DC-link voltage close to 1 pu throughout the frequency excursion, with only a brief shallow dip to 0.97 pu at approximately 4 s. In contrast, MPC permits greater energy extraction from the DC link and, hence, a deeper sag in voltage to 0.90 pu at approximately 8 s. In line with this, Figure 10b shows that PI control allows the rotational speed to fall significantly below the 0.85 pu soft constraint, as energy from the rotating mass is extracted to satisfy grid-side power demand. The rotational speed reaches a minimum of 0.77 pu at approximately 12 s and recovers more slowly. Under MPC, the rotational speed is maintained at a higher value, with a minimum speed of 0.85 pu at approximately 10 s, only marginally below the soft constraint, before recovering more quickly to the nominal speed. This indicates that compared with the PI controller, the MPC allocates more initial transient energy to the DC link, sharing the burden with kinetic energy extraction while the turbine has not yet effectively increased mechanical power. The profiles of MSC power $P_e$ and mechanical power $P_m$ shown in Figure 11 further explain this energy allocation behaviour.

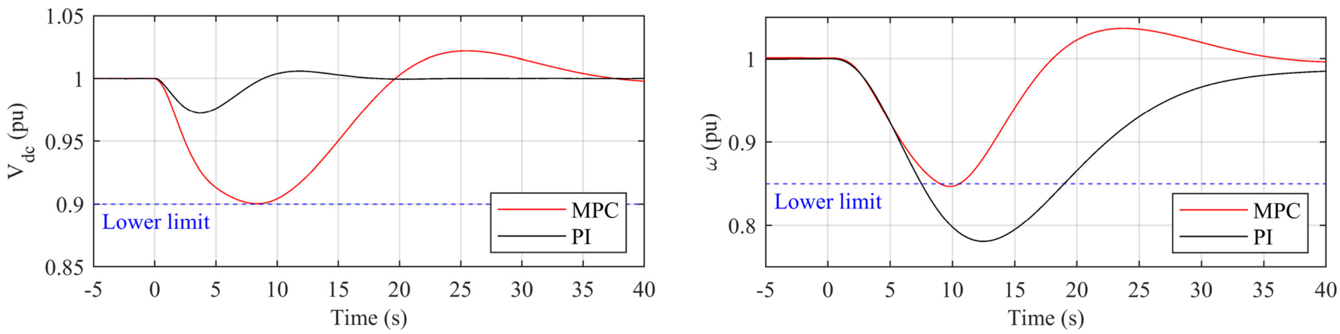


(**a**) (**b**)

**Figure 10.** (**a**) Converter DC-link voltage, $V_{dc}$, and (**b**) machine rotational speed, $\omega$, during the frequency contingency event, comparing responses for MPC and PI control.

Figure 11 highlights how MPC enables improved coordination between the electrical and hydraulic subsystems. For the PI control approach, the DC-link voltage control loop regulates $V_{dc}$ rigidly (Figure 10a), causing the MSC power $P_e$ to rise rapidly (Figure 11a), which is sourced from the synchronous generator. This, in turn, leads to a decrease in rotational speed while the DC-link voltage starts to recover after approximately 4 s. The PI-based governor subsequently reacts to the speed deviation by opening the guide vane, as seen in Figure 11c. However, due to the non-minimum phase behaviour and delay in the hydraulic system, mechanical power $P_m$ can only effectively increase after approximately 7 s, as shown in Figure 11b. This prolongs the period in which kinetic energy is heavily drawn upon by the MSC. This lack of strategic coordination between the two independent control loops leads to a significantly lower minimum speed.

The MPC approach, on the other hand, provides coordination of the control loops and enables proactive control actions, allowing output constraints to be accounted for explicitly. Figure 11a illustrates how the MPC first commands a more gradual rise in MSC power $P_e$, so that the DC link covers more of the immediate energy deficit, thereby reducing deceleration and speed deviation on the machine's rotor and turbine. Meanwhile, the MPC opens the guide vane faster than PI control, yet always within the 0.05 pu/s ramp-rate limit (Figure 11c). As a result, the mechanical power engages early, alongside the less aggressive MSC power extraction, to share the transient load. In Figure 11b, it can be seen that MPC provides a fast and well-controlled rise in mechanical power, $P_m$.

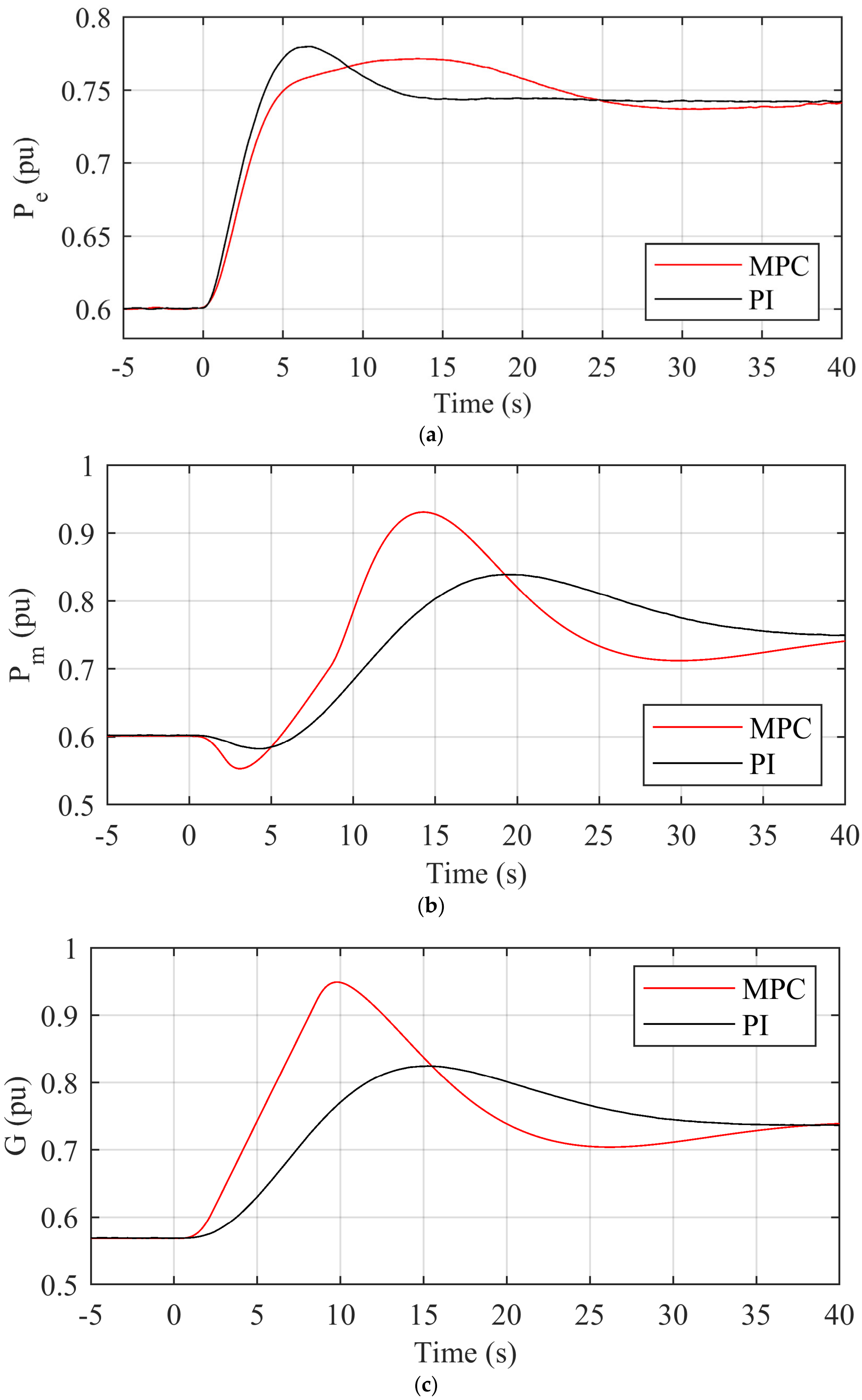


**Figure 11.** Dynamics of internal plant power and guide-vane motion: (**a**) MSC power, $P_e$; (**b**) mechanical power, $P_m$; (**c**) guide-vane opening, $G$.

To quantify the coordination between electrical and hydraulic systems, the energy released by the DC link and that from the rotor during the first swing, defined as the period until the DC-link voltage and the rotational speed reach their respective first minimum values, are examined for both PI and MPC approaches. Figure 12 shows the cumulative energy released by each source of energy, computed by numerical integration of the difference between instantaneous input and output powers for each element during this initial first-swing period, thus focusing on the critical time immediately after the contingency. During the first swing, the MPC approach releases 19 MJ from the DC link and 98 MJ from the rotating mass. In comparison, the PI approach releases 6 MJ and 134 MJ, respectively. In terms of the share of total released energy from these two internal sources, the MPC approach supplies approximately 16% through the DC link and 84% through stored kinetic energy. In contrast, PI control relies mostly on the rotating mass, which supplies 96% of the released energy. This further highlights the MPC approach's ability to shift the transient burden towards the electrical storage element and away from the rotor, thus contributing to maintaining speed closer to its safe operating limits. The MPC approach also results in a smaller total amount of energy being required from these two internal sources (117 MJ compared to 140 MJ for PI), since this approach activates the guide-vane opening faster to achieve an earlier and faster effective mechanical power increase. This observation is also supported by Figure 11b, where integrating the difference between the MPC and PI mechanical power responses over the first-swing interval gives approximately 57 MJ of additional mechanical energy under MPC. Overall, the DC link provides an additional fast energy contribution during the early transient, while the improved mechanical power response provides a larger cumulative energy contribution over the first swing.

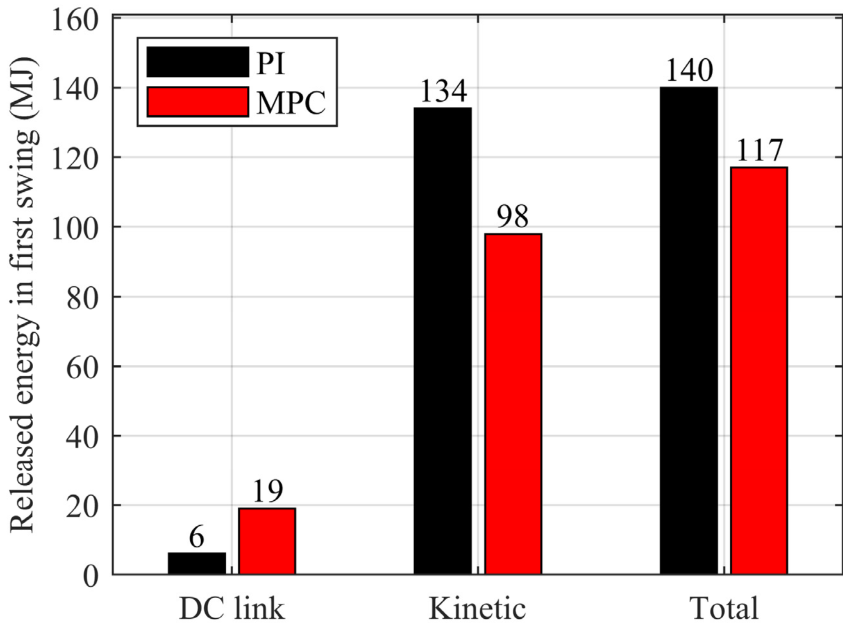


**Figure 12.** Energy released during the first swing: electrical energy provided by the DC link, kinetic energy provided via the rotating mass, and total energy provided.

To clarify the interpretation of the mechanical and hydraulic quantities, additional key plant quantities are calculated from the simulation, as shown in Table 5. With MPC, the minimum rotational speed increases, indicating that the rotational speed is maintained closer to the lower soft bound. The faster engagement of the guide-vane action is also associated with a reduction in the peak torque imbalance from 0.21 pu to 0.18 pu. The peak turbine head variation increases from 0.11 pu to 0.16 pu, reflecting the more active hydraulic response introduced by the earlier guide-vane action. A detailed assessment of cavitation risk, torsional loading, and penstock pressure stress would require dedicated hydraulic and mechanical models or practical measurements. Such analysis is typically used to define acceptable operating regions or constraint limits for a specific machine. In this study, the related quantities are therefore treated as control-relevant operating indicators, rather than as direct measures of component-level stress.

**Table 5.** Additional post-processed indicators.

| Metrics | PI | MPC |
|---|---|---|
| Minimum rotational speed, pu | 0.78 | 0.85 |
| Peak torque imbalance, pu | 0.21 | 0.18 |
| Peak head variation, pu | 0.11 | 0.16 |

As discussed in Section 2.4, the independent PI loops have been tuned to yield adequate gain and phase margins to ensure a stable response. Retuning to accelerate mechanical power ramping and decelerate the DC-link voltage recovery risks reducing phase margin, leading to instability under large disturbances. Alternatives to retuning conventional PI to enable relaxation of DC-link voltage regulation and more aggressive guide-vane response include the incorporation of feedforward compensation and gain-scheduled or adaptive PI. However, each of these approaches requires a high-level coordination layer, with additional switching logic, tuning rules and constraint handling. The principal advantage of MPC is that these interactions are handled within a unified framework.

Overall, the predictive and constraint-aware nature of MPC enables a coordinated use of the available energy sources, allowing the plant to deliver fast frequency support while staying within its safe operating limits.

### *3.2. MPC Robustness Against Plant Model Uncertainty*

MPC is a proactive control scheme capable of providing improved performance compared to conventional reactive control schemes, owing to the control architecture itself incorporating an internal prediction model of the plant under control. This enables the anticipation of future outcomes and optimal control actions accordingly. Consequently, the accuracy of the prediction model and the robustness of the control scheme with underlying uncertainties are paramount. In this study, the proposed MPC is designed using a linear prediction model of the plant that, as demonstrated in the previous section, performs well when applied to the full nonlinear plant. However, in practice, system knowledge is often imperfect or incomplete, measurements are subject to measurement noise, and complex physical dynamics are not always captured across all operating conditions. Hence, it is necessary to assess its performance under such conditions. In this section, we evaluate the robustness of the proposed MPC control against both significant plant-model mismatch and measurement noise.

Two stress conditions are applied simultaneously to the plant, while the linear plant model inside the MPC remains unchanged. First, the stored energy is reduced by lowering both the equivalent DC-link capacitance and the rotational inertia, thus creating a conservative case with smaller energy buffers and a greater mismatch between model and plant. Using this approach, we can examine whether the MPC can still effectively coordinate the internal energy releases when available energy is considerably less in practice than the MPC anticipates. Second, measurement noise is added to each of the plant outputs, thus testing the estimator's performance under degraded sensing conditions.

Specifically, the equivalent DC-link capacitance is reduced by 10%, the rotational inertia constant is reduced by 15%, and all measured outputs are superimposed with white noise of $\pm 2\%$ amplitude relative to their nominal values, as shown in Figure 13. This combination represents a conservative stress case where model uncertainty and sensor noise act concurrently on the prediction and state estimation, respectively.

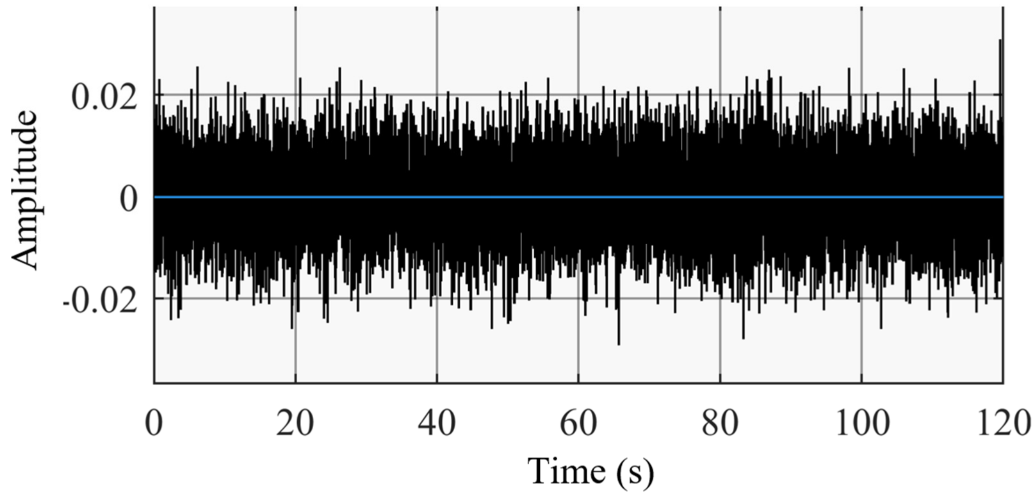


**Figure 13.** Measurement noise added to each of the plant outputs.

With the same grid frequency disturbance and respective response of the GSC shown in Figure 9, the results in Figures 14 and 15 demonstrate that the MPC maintains stable operation, without the need for any MPC retuning. As expected, the reduced inertia and capacitance lower the available energy for frequency support, leading to larger excursions in the DC-link voltage and the rotational speed. The DC-link voltage minimum is slightly reduced (from 0.90 pu to 0.88 pu) compared to the case where an accurate plant model is available, while rotational speed drops more noticeably (from 0.85 pu to 0.82 pu). The DC-link voltage is corrected more rapidly because the electrical subsystem has a shorter response time, while the governor cannot open the guide vane any faster to correct the speed due to its physical rate limit. The MPC therefore allows a deeper speed violation as the least costly solution. Despite this, the MPC continues to balance the energy release effectively, indicating that the prediction and optimisation framework maintains stable operation under the tested parameter variations.

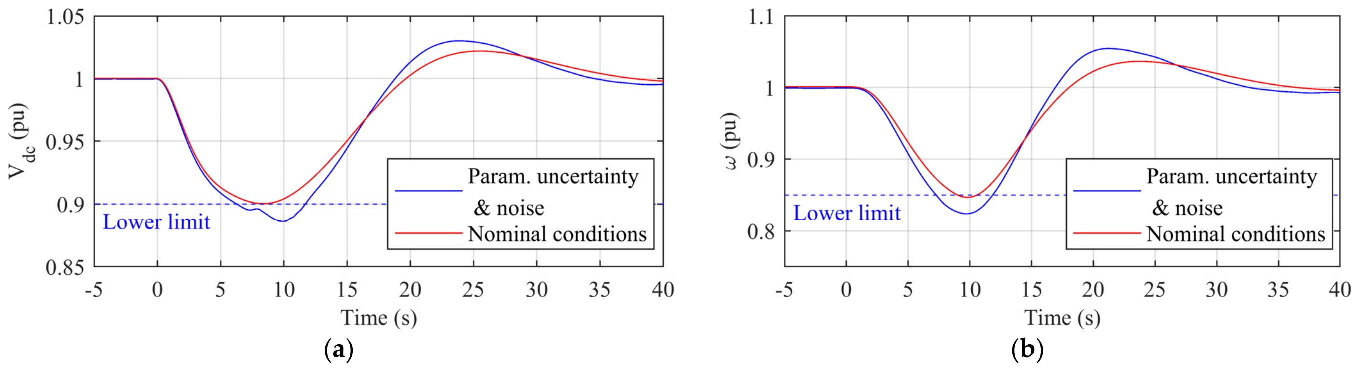


**Figure 14.** DC-link voltage and rotational speed during power increase to the grid, with plant-model mismatch and measurement noise: (**a**) DC-link voltage $V_{dc}$; (**b**) rotational speed $\omega$.

The MPC state estimator remains reliable despite the presence of significant measurement noise. Interestingly, minor actuator jitters can be observed (Figure 15a). This is owing to the limited 20 Hz sampling frequency of the MPC (corresponding to the control time step of 0.05 s), which causes aliasing of high-frequency noise. In this simulation, noisy measurement signals are fed directly to the state estimator without any preprocessing. Despite this, the closed-loop system remains stable under stochastic excitation. This demonstrates that the MPC state estimator is robust to measurement noise even without any signal conditioning. In practical conditions, measurement signals typically go through low-pass filters before entering the estimator. Such filtering, with a bandwidth below the MPC's Nyquist frequency, would further suppress high-frequency noise without compromising observability.

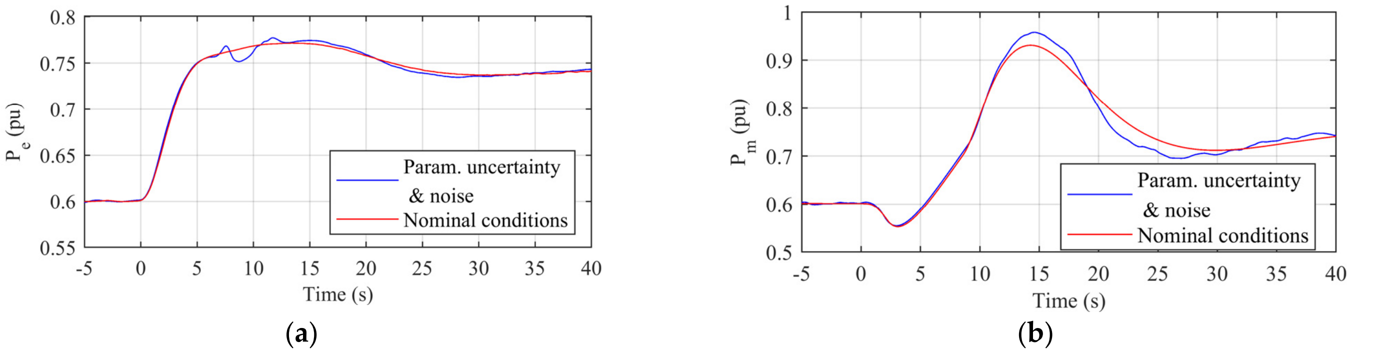


**Figure 15.** Dynamics of internal plant power under plant-model mismatch and measurement noise conditions: (**a**) MSC power $P_e$; (**b**) mechanical power $P_m$.

### *3.3. Impact of Extended DC-Link Energy Buffers on Frequency Support Under Aggressive Droop Control*

In this case study we evaluate the performance of the PHS system when it is controlled to provide more aggressive primary frequency response. The droop setting is reduced from 0.04 to 0.02. A lower droop coefficient demands a significantly larger and faster active power injection into the grid to arrest the grid frequency disturbance, which is typically provided by fast converter-interfaced resources such as battery energy storage systems [45]. The response of the proposed MPC-controlled PHS plant with this demanding droop setting is shown by the red traces in Figure 16. It can be seen that the DC-link voltage drops to 0.87 pu and the rotational speed drops to 0.80 pu, significantly below their respective soft constraints. Providing a quicker and larger injection of power, corresponding to the more aggressive droop settings, requires rapid energy delivery that cannot be fully met by the hydraulic system, since it is already operating at its maximum ramping capability. The MPC extracts the required additional energy from the DC link and the machine rotor, effectively sharing the burden between them. However, under this scenario the rate-limited hydraulic response forces greater reliance on electrical and mechanical energy buffers, leading to the observed drop in both DC-link voltage and rotational speed below their respective lower soft constraints.

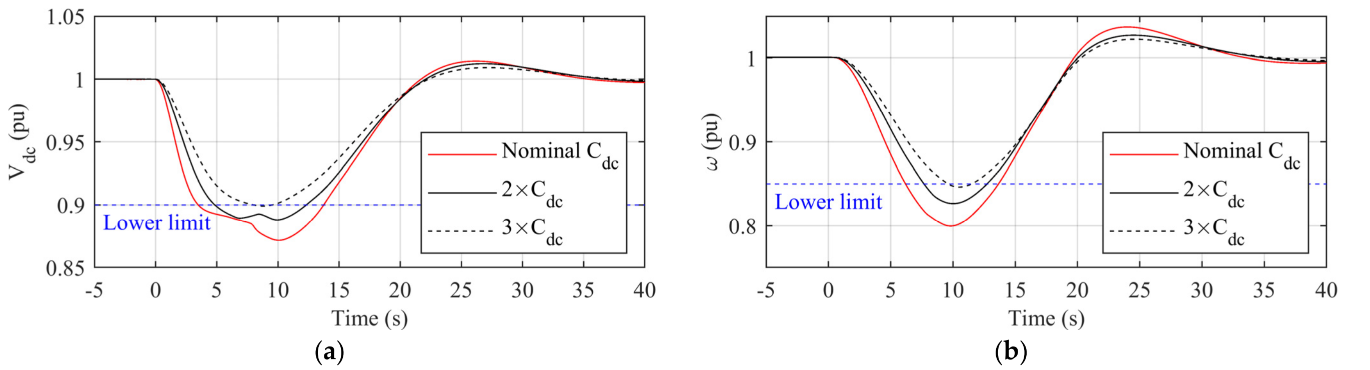


**Figure 16.** System transient response under an aggressive frequency droop setting with varying DC-link energy capacities: (**a**) DC-link voltage; (**b**) rotational speed.

A sensitivity study is performed to investigate a candidate option for mitigation of soft-constraint violations under aggressive droop scenarios, in which the available DC-link energy storage is expanded. The simulated scenarios represent a doubling and tripling of the equivalent DC-link capacitance; this could be practically realised through the integration of a supercapacitor interfaced via a dedicated DC-DC converter directly into the existing DC link. Figure 17 quantifies how the MPC coordinates this extended buffer to shift part of the transient energy burden away from the rotating mass. During the critical first swing, the nominal setup releases 24 MJ from the DC link, requiring the rotating mass to supply 124 MJ of kinetic energy. By doubling the equivalent DC storage, the DC link provides 44 MJ, reducing the kinetic energy burden to 109 MJ. In the tripled case, the DC link provides up to 58 MJ, significantly lowering the kinetic demand to just 97 MJ, and as shown in Figure 16, with the DC-link storage tripled, the rotational speed and DC-link voltage remain within their limits. It is worth noting that for previously evaluated disturbances (Section 3.1), the proactive coordination of the MPC reduced the total energy released by accelerating the hydraulic response, without violating soft constraints. However, under this more aggressive droop scenario, the hydraulic system operates near its limit across all scenarios. Because the hydraulic system is at its physical ramp limit and cannot accelerate further, the total energy released increases slightly (from 148 MJ to 155 MJ). This reflects how the extended DC storage provides the extra energy required by the grid, compensating for the saturated hydraulic system and relaxing the transient burden on the rotating mass.

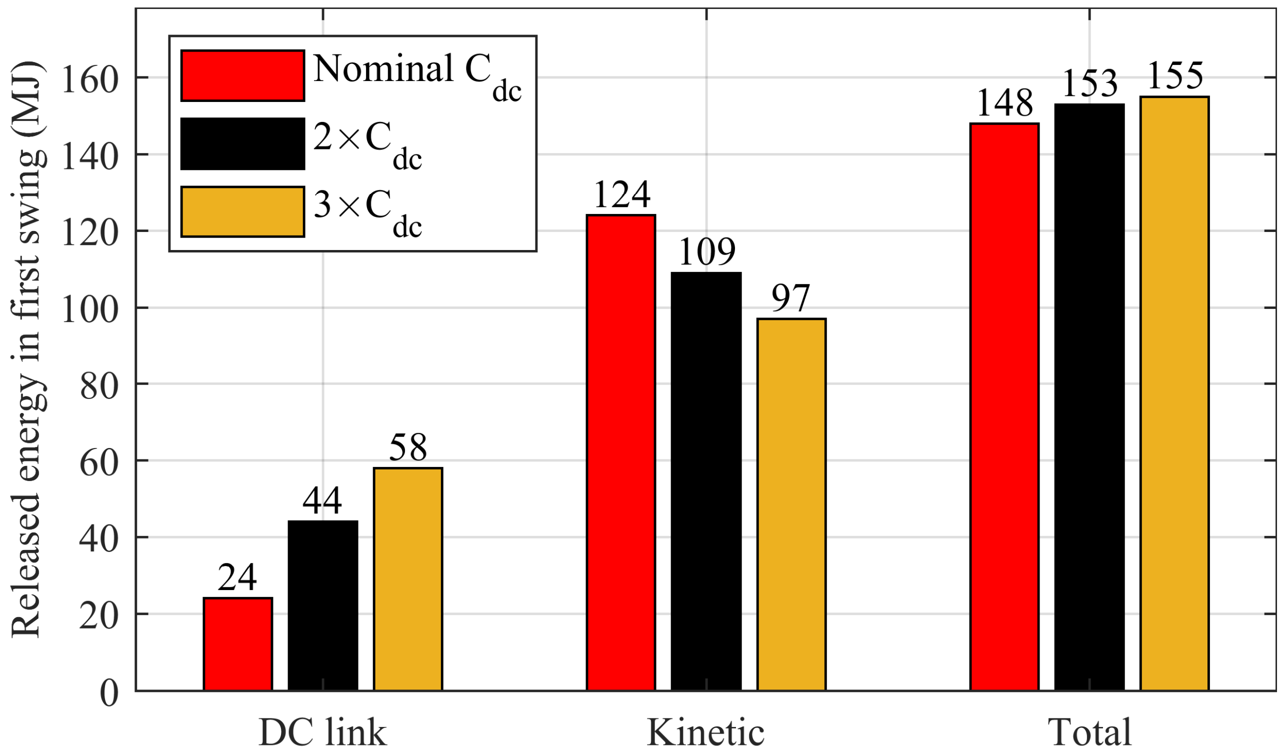


**Figure 17.** Impact of extended equivalent DC-link capacitance on primary frequency response, illustrating how extended DC-link buffer scenarios (×2, ×3) reduce kinetic energy extraction from the rotating mass.

It can be seen that with extended short-duration, fast-release storage connected to the DC link, the VS-PHS units may have more flexibility in managing the constraints. In a practical context, industrial grid stabilisation products already use supercapacitor-based short-duration energy support at the scale of hundreds of MJ, with activation delays of milliseconds after disturbance detection [46]. This indicates that the short-duration energy range considered in this study is technically plausible, although the specific sizing for VS-PHS remains site- and service-dependent.

To further demonstrate the coordination capabilities of the proposed controller, an even more demanding stress test featuring a highly aggressive 1% droop setting (0.01) and a five-fold expansion of the equivalent DC-link energy buffer was investigated. Figure 18 illustrates the system's transient response under these conditions. Despite the large and rapid active power injection required by the 1% droop, the MPC manages the transient response near the soft constraints.

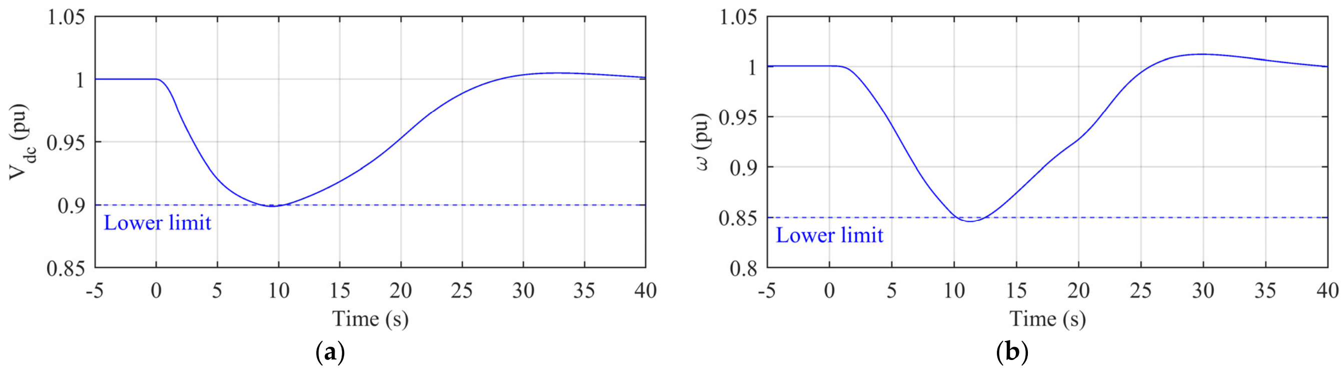


**Figure 18.** System transient response with an extreme 1% frequency droop setting and with a 5× extended DC-link storage capacity: (**a**) DC-link voltage; (**b**) rotational speed.

Overall, these simulations suggest that providing rapid power response from pumped storage systems can, under some scenarios, be bottlenecked by the physical limitations of the hydraulic system, since long penstocks and strict mechanical actuator limits make it difficult to safely accelerate the water column to meet rapid changes in grid demand. Since improving the hydraulic response generally requires major waterway or mechanical upgrades, which can be impractical or expensive depending on the site, additional solutions are needed if more aggressive power injection for frequency support is desired. The results of this study suggest that expanding the internal DC-link energy storage, together with the proposed MPC framework, can provide a complementary option for reducing dependence on rotor kinetic energy during aggressive frequency-support conditions, particularly when the hydraulic system has reached its performance limits. The MPC approach, together with extended DC-link storage, provides PHS designers and operators with the opportunity to deliver fast frequency response without the need for major hydraulic system redesign to accommodate it. The applicability of the MPC approach and a PHS system's suitability for providing this service depend on plant topology, topographical conditions, hydraulic constraints, and the frequency-support service expected from the unit.

## 4. Conclusions

In this paper, we propose a model predictive control approach to enable rapid primary frequency response in variable-speed pumped hydro storage systems. This study focuses on challenging VS-PHS scenarios where slow hydraulic response limits the ability of conventional control to provide fast changes in electrical power output. The proposed MPC preserves the grid-side droop-based PFC response and replaces the independent turbine governor and the DC-link voltage control loops, using predictions and explicit constraints to coordinate the DC link, the rotating mass, and the hydraulic system. Compared with conventional PI control, which rigidly maintains the DC link and forces the rotor to supply most of the initial transient energy via rapid speed reduction before the turbine increases mechanical power, the MPC allocates the transient energy contribution more deliberately.

In a predictive and constraint-aware manner, the MPC allows the DC link to share more of the early transient burden, while the guide-vane response is activated proactively to mitigate the effect of slow hydraulic response and actuator limits.

The robustness study indicates that the MPC maintains stable operation under significant plant-model mismatch and in the presence of measurement noise. The extended DC-link storage study shows that the MPC can manage the operating constraints under more aggressive primary frequency control commitments when additional short-duration electrical storage is available. This may provide a complementary option to be considered alongside hydraulic system upgrades when demanding grid support is required.

**Author Contributions:** Conceptualisation, K.N., E.F., M.N., A.H. and W.H.; methodology, K.N. and E.F.; software, K.N.; writing—original draft preparation, K.N., E.F., M.N., A.H. and W.H.; writing—K.N., E.F., M.N., A.H. and W.H.; visualisation, K.N., E.F., M.N., A.H. and W.H.; supervision, E.F., M.N. and A.H.; project administration, E.F.; funding acquisition, E.F., M.N., A.H. and W.H. All authors have read and agreed to the published version of the manuscript.

**Funding:** This research was funded by the Australian Research Council in Energy Technologies for Future Grids, grant number IC210100021.

**Data Availability Statement:** The original contributions presented in this study are included in the article. Further enquiries can be directed to the corresponding author.

**Conflicts of Interest:** The authors declare no conflicts of interest.

## Abbreviations and Notations

The following abbreviations and notations are used in this manuscript:

| | |
|---|---|
| PHS | Pumped hydro storage |
| VS-PHS | Variable-speed pumped hydro storage |
| MPC | Model predictive control |
| PI | Proportional–integral |
| MSC | Machine-side converter |
| GSC | Grid-side converter |
| DC | Direct current |
| AC | Alternating current |
| PFC | Primary frequency control |
| PCC | Point of common coupling |
| VSC | Voltage-source converter |
| $dq$ | Synchronous rotating reference frame |
| $abc$ | Three-phase stationary frame |
| PWM | Pulse-width modulation |
| QP | Quadratic programming |
| pu | Per unit |
| $G$ | Guide-vane opening |
| $q$ | Flow into the pump-turbine |
| $h$ | Turbine head |
| $h_r$ | Rated turbine head |
| $f_p$ | Head loss coefficient |
| $\omega$ | Rotational speed |
| $\Delta\omega$ | Rotational speed deviation |
| $\eta$ | Turbine efficiency |
| $P_m$ | Mechanical power of the turbine |
| $P_e$ | Electrical power supplied by the MSC to the DC link |
| $P_g$ | Electrical power delivered by GSC to the grid |
| $V_{dc}$ | DC-link voltage |

| | |
|---|---|
| $I_m$ | Generator current controlled by MSC |
| $I_g$ | Grid injection current regulated by GSC |
| $T_w$ | Water starting time constant |
| $H_m$ | Machine inertia constant |
| $D_m$ | Mechanical damping coefficient |
| $T_g$ | Hydraulic servomotor time constant |
| $T_e$ | Wave travel time |
| $T_c$ | Current control loop time constant |
| $C_{dc}$ | Equivalent DC-link capacitance |
| $R_{dc}$ | DC-link shunt leakage resistance |
| $K$ | Voltage ratio |
| $\hat{\cdot}$ | Indicates estimation or prediction |
| $\cdot^*$ | Indicates reference value |
| $\cdot_{dq}$ | Variable on the $dq$ axes |
| $G_{max}$,$G_{min}$ | Maximum and minimum guide-vane opening bounds |
| $R_{G,max}$ | Maximum guide-vane opening rate |
| $R_{I,max}$ | Maximum MSC current rate |
| $N_p$ | MPC prediction horizon |
| $N_c$ | MPC control horizon |
| $J$ | Cost function |
| $M$ | Kalman gain matrix |
| $w_k$ | Process noise sequence |
| $v_k$ | Measurement noise sequence |
| $T_s$ | MPC time step |
| $x_k$ | State vector |
| $u_k$ | Plant input vector |
| $y_k$ | Measured output vector |
| $r_k$ | Reference vector |
| $\Delta u$ | Input increment vector |
| $\varepsilon_k$ | Slack variable |
| $W_y$ | Output weight matrix |
| $W_\Delta$ | Input rate weight matrix |
| $\rho$ | Soft-constraint violation weight |
| $d_k$ | Disturbance state vector |
| $A$, $B$, $C$ | System matrices of the plant |
| $B_d$ | Input-disturbance matrix |
| $C_d$ | Output-disturbance matrix |
| $A_g$, $B_g$, $C_g$, $D_g$ | State-space matrices of the hydraulic servomotor |
| $A_h$, $B_h$, $C_h$, $D_h$ | State-space matrices of the penstock–turbine system |
| $A_\omega$, $B_\omega$, $C_\omega$, $D_\omega$ | State-space matrices of the rotating speed dynamics |
| $A_c$, $B_c$, $C_c$, $D_c$ | State-space matrices of the converter current control loops |
| $A_v$, $B_v$, $C_v$, $D_v$ | State-space matrices of the converter DC-link voltage dynamics |

## Appendix A

*Appendix A.1 State-Space Model of the Servomotor*

State: $[g]$.

System matrices: $A_g = \left[-\frac{1}{T_g}\right], B_g = [1], C_g = \left[\frac{1}{T_g}\right],\ D_g = [0]$.

*Appendix A.2 Penstock and Turbine*

State: $\begin{bmatrix} h_1 \\ h_2 \\ h_3 \end{bmatrix}$.

System matrices:

$$A_h = \begin{bmatrix} -650.9 & -7.559 \times 10^4 & -5.92 \times 10^4 \\ 1 & 0 & 0 \\ 0 & 1 & 0 \end{bmatrix}, B_h = \begin{bmatrix} 1 \\ 0 \\ 0 \end{bmatrix},$$

$$C_h = \begin{bmatrix} 450 & -1.294 \times 10^5 & 5.071 \times 10^4 \end{bmatrix}, D_h = [0].$$

*Appendix A.3 Synchronous Machine*

State: $[\Delta\omega]$.

System matrices: $A_\omega = \begin{bmatrix} -\frac{D_m}{2H_m} \end{bmatrix}, B_\omega = \begin{bmatrix} \frac{1}{2H_m} & -\frac{1}{2H_m} \end{bmatrix}, C_\omega = [1], D_\omega = \begin{bmatrix} 0 & 0 \end{bmatrix}.$

*Appendix A.4 Converter Current Control*

State: $\begin{bmatrix} i_{md} \\ i_{gd} \end{bmatrix}$

System matrices: $A_c = \begin{bmatrix} -\frac{1}{T_c} & 0 \\ 0 & -\frac{1}{T_c} \end{bmatrix}, B_c = \begin{bmatrix} 1 & 0 \\ 0 & 1 \end{bmatrix}, C_c = \begin{bmatrix} \frac{1}{T_c} & 0 \\ 0 & \frac{1}{T_c} \end{bmatrix}, D_c = \begin{bmatrix} 0 & 0 \\ 0 & 0 \end{bmatrix}.$

*Appendix A.5 Converter DC-Link Voltage*

State: $[v_{dc}]$

System matrices: $A_v = \begin{bmatrix} -\frac{1}{R_{dc}C_{dc}} \end{bmatrix}, B_v = \begin{bmatrix} K & -K \end{bmatrix}, C_v = [1], D_v = \begin{bmatrix} 0 & 0 \end{bmatrix}.$

*Appendix A.6 Discrete Prediction Model*

State $\begin{bmatrix} g, h_1, h_2, h_3, \Delta\omega_m, i_{md}, v_{dc}, i_{gd} \end{bmatrix}^T$.

System matrices:

$$A = \begin{bmatrix} 6.065 \times 10^{-1} & 0 & 0 & 0 & 0 & 0 & 0 & 0 \\ -9.331 \times 10^{-4} & -2.287 \times 10^{-4} & -1.133 \times 10^{-1} & 5.085 \times 10^{-1} & 0 & 0 & 0 & 0 \\ 8.473 \times 10^{-5} & -8.589 \times 10^{-6} & -5.820 \times 10^{-3} & -7.626 \times 10^{-1} & 0 & 0 & 0 & 0 \\ 4.409 \times 10^{-6} & 1.288 \times 10^{-5} & 8.377 \times 10^{-3} & 9.679 \times 10^{-1} & 0 & 0 & 0 & 0 \\ -7.532 \times 10^{-2} & -2.347 \times 10^{-1} & -2.168 \times 10^{2} & 9.008 \times 10^{2} & 9.996 \times 10^{-1} & -1.419 \times 10^{-1} & 0 & 0 \\ 0 & 0 & 0 & 0 & 0 & 6.738 \times 10^{-3} & 0 & 0 \\ 0 & 0 & 0 & 0 & 0 & 6.530 \times 10^{-1} & 1 & -6.530 \times 10^{-1} \\ 0 & 0 & 0 & 0 & 0 & 0 & 0 & 6.738 \times 10^{-3} \end{bmatrix},$$

$$B = \begin{bmatrix} 3.935 \times 10^{-2} & 0 \\ 8.473 \times 10^{-5} & 0 \\ 4.409 \times 10^{-6} & 0 \\ 1.007 \times 10^{-7} & 0 \\ -1.566 \times 10^{-3} & -5.723 \times 10^{-3} \\ 0 & 9.933 \times 10^{-3} \\ 0 & 2.634 \times 10^{-2} \\ 0 & 0 \end{bmatrix}, C = \begin{bmatrix} 10 & 0 & 0 & 0 & 0 & 0 & 0 & 0 \\ 0 & 450 & -1.294 \times 10^5 & 5.071 \times 10^4 & 0 & 0 & 0 & 0 \\ 0 & 0 & 0 & 0 & 1 & 0 & 0 & 0 \\ 0 & 0 & 0 & 0 & 0 & 100 & 0 & 0 \\ 0 & 0 & 0 & 0 & 0 & 0 & 1 & 0 \end{bmatrix}, B_d = \begin{bmatrix} 0 & 0 \\ 0 & 0 \\ 0 & 0 \\ 0 & 0 \\ 0 & 0 \\ 0 & 0 \\ -2.634 \times 10^{-2} & 0 \\ 9.933 \times 10^{-3} & 0 \end{bmatrix}, C_d = \begin{bmatrix} 0 & 0 \\ 0 & 0 \\ 0 & 1 \\ 0 & 0 \\ 0 & 0 \end{bmatrix}.$$

*Appendix A.7 State Estimator Gain Matrix*

$$M = \begin{bmatrix} 1.290 \times 10^{-2} & -1.691 \times 10^{-2} & -1.237 \times 10^{-4} & -3.544 \times 10^{-7} & -1.133 \times 10^{-7} \\ 1.698 \times 10^{-5} & -2.000 \times 10^{-5} & 1.736 \times 10^{-7} & 4.965 \times 10^{-10} & 2.677 \times 10^{-10} \\ 1.432 \times 10^{-6} & -2.130 \times 10^{-6} & -1.416 \times 10^{-8} & -4.049 \times 10^{-11} & -1.824 \times 10^{-11} \\ 1.679 \times 10^{-7} & 7.810 \times 10^{-8} & -4.690 \times 10^{-9} & -1.354 \times 10^{-11} & 1.255 \times 10^{-12} \\ -1.706 \times 10^{-3} & 1.030 \times 10^{-3} & 4.756 \times 10^{-4} & -2.872 \times 10^{-3} & -1.257 \times 10^{-5} \\ -3.544 \times 10^{-8} & 4.777 \times 10^{-8} & -2.722 \times 10^{-5} & 4.965 \times 10^{-3} & 1.243 \times 10^{-4} \\ -1.133 \times 10^{-6} & 2.545 \times 10^{-6} & -7.535 \times 10^{-4} & 1.243 \times 10^{-2} & 5.988 \times 10^{-2} \\ -7.238 \times 10^{-8} & -9.595 \times 10^{-8} & -7.839 \times 10^{-6} & 6.409 \times 10^{-6} & -4.847 \times 10^{-4} \\ -7.238 \times 10^{-6} & -9.595 \times 10^{-6} & -7.839 \times 10^{-4} & 6.409 \times 10^{-4} & -4.847 \times 10^{-2} \\ 4.691 \times 10^{-4} & 6.431 \times 10^{-4} & 4.874 \times 10^{-2} & 1.503 \times 10^{-4} & -7.409 \times 10^{-4} \end{bmatrix}.$$

## References


1. Meng, L.; Zafar, J.; Khadem, S.K.; Collinson, A.; Murchie, K.C.; Coffele, F.; Burt, G.M. Fast Frequency Response from Energy Storage Systems—A Review of Grid Standards, Projects and Technical Issues. *IEEE Trans. Smart Grid* **2020**, *11*, 1566–1581. [CrossRef]
2. Blakers, A.; Weber, T.; Silalahi, D. Pumped hydro energy storage to support 100% renewable energy. *Prog. Energy* **2025**, *7*, 022004. [CrossRef]
3. Christe, A.; Faulstich, A.; Vasiladiotis, M.; Steinmann, P. World's First Fully Rated Direct ac/ac MMC for Variable-Speed Pumped-Storage Hydropower Plants. *IEEE Trans. Ind. Electron.* **2023**, *70*, 6898–6907. [CrossRef]
4. Steimer, P.K.; Senturk, O.; Aubert, S.; Linder, S. Converter-fed synchronous machine for pumped hydro storage plants. In Proceedings of the 2014 IEEE Energy Conversion Congress and Exposition (ECCE), Pittsburgh, PA, USA, 14–18 September 2014; pp. 4561–4567.
5. Valavi, M.; Nysveen, A. Variable-Speed Operation of Hydropower Plants: A Look at the Past, Present, and Future. *IEEE Ind. Appl. Mag.* **2018**, *24*, 18–27. [CrossRef]
6. Nobile, E.; Sari, G.; Schwery, A. Variable Speed Hydro Pumped Storage as Flexible Enabler of Intermittent Renewable Penetration. In Proceedings of the 2018 IEEE Power & Energy Society General Meeting (PESGM), Portland, OR, USA, 5–10 August 2018; pp. 1–5.
7. Nguyen, K.; Franklin, E.; Negnevitsky, M.; Henderson, A.; Hassan, W.; Hosseinabadi, P.A. Frequency Control in Hydro Power Systems with High Penetration of Inverter-Based Resources. *IEEE Trans. Ind. Appl.* **2026**, 1–11. [CrossRef]
8. Trivedi, C.; Iliev, I.; Dahlhaug, O.G.; Markov, Z.; Engstrom, F.; Lysaker, H. Investigation of a Francis turbine during speed variation: Inception of cavitation. *Renew. Energy* **2020**, *166*, 147–162. [CrossRef]
9. Liu, X.; Luo, Y.; Wang, Z. A review on fatigue damage mechanism in hydro turbines. *Renew. Sustain. Energy Rev.* **2016**, *54*, 1–14. [CrossRef]
10. Mennemann, J.F.; Marko, L.; Schmidt, J.; Kemmetmüller, W.; Kugi, A. Nonlinear Model Predictive Control of a Variable-Speed Pumped-Storage Power Plant. *IEEE Trans. Control Syst. Technol.* **2021**, *29*, 645–660. [CrossRef]
11. Cassano, S.; Sossan, F. Model predictive control for a medium-head hydropower plant hybridized with battery energy storage to reduce penstock fatigue. *Electr. Power Syst. Res.* **2022**, *213*, 108545. [CrossRef]
12. Santosuosso, L.; Camal, S.; Lett, A.; Bontron, G.; Kariniotakis, G. Distributed economic model predictive control for the joint energy dispatch of wind farms and run-of-the-river hydropower plants. *Electr. Power Syst. Res.* **2024**, *235*, 110805. [CrossRef]
13. Ersdal, A.M.; Imsland, L.; Uhlen, K. Model Predictive Load-Frequency Control. *IEEE Trans. Power Syst.* **2016**, *31*, 777–785. [CrossRef]
14. Bulatov, Y.N.; Kryukov, A.V.; Suslov, K.V. Group predictive voltage and frequency regulators for small hydro power plant in the context of low power quality. *Renew. Energy* **2022**, *200*, 571–578. [CrossRef]
15. Jin, C.; Li, W.; Shen, J.; Li, P.; Liu, L.; Wen, K. Active Frequency Response Based on Model Predictive Control for Bulk Power System. *IEEE Trans. Power Syst.* **2019**, *34*, 3002–3013. [CrossRef]
16. He, J.; Shi, C.; Wei, T.; Jia, D. Stochastic Model Predictive Control of Hybrid Energy Storage for Improving AGC Performance of Thermal Generators. *IEEE Trans. Smart Grid* **2022**, *13*, 393–405. [CrossRef]
17. Zhu, J.; Cui, X.; Ni, W. Model predictive control based control strategy for battery energy storage system integrated power plant meeting deep load peak shaving demand. *J. Energy Storage* **2022**, *46*, 103811. [CrossRef]
18. Long, B.; Liao, Y.; Chong, K.T.; Rodríguez, J.; Guerrero, J.M. MPC-Controlled Virtual Synchronous Generator to Enhance Frequency and Voltage Dynamic Performance in Islanded Microgrids. *IEEE Trans. Smart Grid* **2021**, *12*, 953–964. [CrossRef]
19. Beus, M.; Pandžić, H. Application of Model Predictive Control Algorithm on a Hydro Turbine Governor Control. In Proceedings of the 2018 Power Systems Computation Conference (PSCC), Dublin, Ireland, 11–15 June 2018; pp. 1–7.
20. Beus, M.; Pandžić, H. Practical Implementation of a Hydro Power Unit Active Power Regulation Based on an MPC Algorithm. *IEEE Trans. Energy Convers.* **2022**, *37*, 243–253. [CrossRef]
21. Yu, X.; Zhao, Q.; Gao, C.; Zhang, L.; Wu, Y.; Nan, H. Generalized Predictive Control of Doubly Fed Variable-Speed Pumped Storage Unit. *Energies* **2025**, *18*, 2904. [CrossRef]
22. Jukić, D.-K.; Kugi, A.; Kemmetmüller, W. Optimal dynamic operation of pumped storage power plants with variable and fixed speed generators. *Control. Eng. Pract.* **2023**, *138*, 105601. [CrossRef]
23. Xu, Z.; Deng, C.; Yang, Q. A primary frequency control strategy for variable-speed pumped-storage plant in generating mode based on adaptive model predictive control. *Electr. Power Syst. Res.* **2023**, *221*, 109356. [CrossRef]
24. Reigstad, T.I.; Uhlen, K. Optimized Control of Variable Speed Hydropower for Provision of Fast Frequency Reserves. *Electr. Power Syst. Res.* **2020**, *189*, 106668. [CrossRef]
25. Reigstad, T.I.; Uhlen, K. Variable Speed Hydropower for Provision of Fast Frequency Reserves in the Nordic Grid. *IEEE Trans. Power Syst.* **2021**, *36*, 5476–5485. [CrossRef]

26. Reigstad, T.I.; Uhlen, K. Nonlinear model predictive control of variable speed hydropower for provision of fast frequency reserves. *Electr. Power Syst. Res.* **2021**, *194*, 107067. [CrossRef]
27. Al Kez, D.; Foley, A.M.; Ahmed, F.; Morrow, D.J. Overview of frequency control techniques in power systems with high inverter-based resources: Challenges and mitigation measures. *IET Smart Grid* **2023**, *6*, 447–469. [CrossRef]
28. Tiwari, R.; Nilsen, R.; Mo, O.; Nysveen, A. Control Methods for Operation of Pumped Storage Plants with Full-Size Back-to-Back Converter Fed Synchronous Machines. *IEEE Trans. Ind. Appl.* **2023**, *59*, 6792–6803. [CrossRef]
29. Working Group on Prime Mover and Energy Supply. Hydraulic turbine and turbine control models for system dynamic studies. *IEEE Trans. Power Syst.* **1992**, *7*, 167–179. [CrossRef]
30. Munoz-Hernandez, G.A.; Mansoor, S.P.; Jones, D.I. *Modelling and Controlling Hydropower Plants*; Springer: New York, NY, USA, 2013.
31. Guo, B.; Mohamed, A.; Bacha, S.; Alamir, M.; Boudinet, C.; Pouget, J. Reduced-Scale Models of Variable Speed Hydro-Electric Plants for Power Hardware-in-the-Loop Real-Time Simulations. *Energies* **2020**, *13*, 5764. [CrossRef]
32. Brezovec, M.; Kuzle, I.; Tomisa, T. Nonlinear digital simulation model of hydroelectric power unit with Kaplan turbine. *IEEE Trans. Energy Convers.* **2006**, *21*, 235–241. [CrossRef]
33. Kranjcic, D.; Štumberger, G. Differential Evolution-Based Identification of the Nonlinear Kaplan Turbine Model. *IEEE Trans. Energy Convers.* **2014**, *29*, 178–187. [CrossRef]
34. *IEEE Std 1110-2019*; IEEE Guide for Synchronous Generator Modeling Practices and Parameter Verification with Applications in Power System Stability Analyses. IEEE: Piscataway, NJ, USA, 2020; pp. 1–92. [CrossRef]
35. D'Arco, S.; Suul, J.A.; Fosso, O.B. Automatic tuning of cascaded controllers for power converters using eigenvalue parametric sensitivities. *IEEE Trans. Ind. Appl.* **2014**, *51*, 1743–1753. [CrossRef]
36. Maeder, U.; Borrelli, F.; Morari, M. Linear offset-free Model Predictive Control. *Automatica* **2009**, *45*, 2214–2222. [CrossRef]
37. AEMO. *Primary Frequency Response Requirements*; Australian Energy Market Operator: Melbourne, VIC, Australia, 2023.
38. Pannocchia, G.; Rawlings, J.B. Disturbance models for offset-free model-predictive control. *AICHE J.* **2003**, *49*, 426–437. [CrossRef]
39. Pannocchia, G.; Bemporad, A. Combined Design of Disturbance Model and Observer for Offset-Free Model Predictive Control. *IEEE Trans. Autom. Control* **2007**, *52*, 1048–1053. [CrossRef]
40. Camacho, E.F.; Bordons, C.; Maestre, J.M. *Model Predictive Control: Third Edition*; Springer: Cham, Switzerland, 2026.
41. MATLAB. *Model Predictive Control Toolbox User's Guide Version 25.2*; The MathWorks, Inc.: Natick, MA, USA, 2025.
42. *IEEE Std 1207-2011*; IEEE Guide for the Application of Turbine Governing Systems for Hydroelectric Generating Units. IEEE: Piscataway, NJ, USA, 2011; pp. 1–131.
43. Sarasúa, J.I.; Pérez-Díaz, J.I.; Wilhelmi, J.R.; Sánchez-Fernández, J.Á. Dynamic response and governor tuning of a long penstock pumped-storage hydropower plant equipped with a pump-turbine and a doubly fed induction generator. *Energy Convers. Manag.* **2015**, *106*, 151–164. [CrossRef]
44. Yang, W.; Yang, J.; Guo, W.; Norrlund, P. Response time for primary frequency control of hydroelectric generating unit. *Int. J. Electr. Power Energy Syst.* **2016**, *74*, 16–24. [CrossRef]
45. Hatziargyriou, N.; Milanovic, J.; Rahmann, C.; Ajjarapu, V.; Canizares, C.; Erlich, I.; Hill, D.; Hiskens, I.; Kamwa, I.; Pal, B.; et al. Definition and Classification of Power System Stability—Revisited & Extended. *IEEE Trans. Power Syst.* **2021**, *36*, 3271–3281. [CrossRef]
46. Hitachi. Hitachi ABB Power Grids Launches SVC Light® Enhanced Solution Accelerating Resilient and Carbon-Neutral Energy Future. Available online: https://www.hitachienergy.com/news-and-events/press-releases/2021/08/hitachi-abb-power-grids-launches-svc-light-enhanced-solution-accelerating-resilient-and-carbon-neutral-energy-future (accessed on 25 June 2026).